Characterizing Ash Properties and Effects on Diesel Particulate Filter Flow Resistance

by

Gregory James Monahan

B.S., Mechanical Engineering
Villanova University, 2014

Submitted to the Department of Mechanical Engineering
in Partial Fulfillment of the Requirements for the Degree of

Masters of Science in Mechanical Engineering

at the

Massachusetts Institute of Technology

June 2016

Signature of Author: _____

Department of Mechanical Engineering
May 18, 2016

Certified by: _____

Victor W. Wong
Principal Research Scientist and Lecturer in Mechanical Engineering
Thesis Supervisor

Accepted by: _____

Rohan Abeyaratne
Professor of Mechanical Engineering
Graduate Officer

(This page intentionally left blank)

Characterizing Ash Properties and Effects on Diesel Particulate Filter Flow Resistance

by

Gregory James Monahan

Submitted to the Department of Mechanical Engineering on May 18, 2016 in Partial Fulfillment
of the Requirements for the Degree of

Masters of Science in Mechanical Engineering

ABSTRACT

As a result of increasingly stringent emissions regulations, Diesel Particulate Filters (DPF) have become a widespread method of reducing particulate emissions in both on and off highway diesel engine use. This particular aftertreatment system is chosen for its high filtration efficiency and relative simplicity. The porous ceramic substrate captures the particulate matter which is comprised of combustible soot and inorganic metallic ash. While the soot can be cleared from the filter through high temperature oxidation, the small amount of ash remains in the filter. The presence of these soot and ash particles creates an increase in the flow resistance of the filter which creates more backpressure on the engine and results in a decrease in fuel economy.

Over the life of the filter, the ash particles become a significant portion of particulate matter in the filter and the resulting flow resistance. While the effects of ash and soot on filter performance have been extensively studied, the underlying deposition mechanisms and effects of various ash properties are not well understood. The focus of this research is to investigate the effects of ash properties such as packing density and chemistry on the flow resistance of both the ash cake layer and the filter substrate. The results of this and other research can support the optimization of operating conditions, regeneration strategies, and lubricant additive formulations for decreased system backpressure.

Additionally, this research seeks to develop and improve advanced diagnostic tools in order to bridge the gap between macro scale quantifiable flow resistance and micro scale deposition characteristics. Using both high resolution X-Ray CT imaging and flow simulation tools, a method is tested by which values for ash and filter permeability can be calculated to investigate local micro scale filter phenomena or various lab and field samples.

Thesis Supervisor: Victor W. Wong
Title: Principal Research Scientist and Lecturer in Mechanical Engineering

(This page intentionally left blank)

ACKNOWLEDGEMENTS

My time at MIT has been a uniquely wonderful opportunity to challenge my own engineering abilities, work with some of the brightest people I have ever met, and find something new to learn every day. It would not have been possible without the support of my family, the faculty, and the many students with whom I have worked.

First, I would like to thank my thesis advisor, Dr. Wong, for giving me the opportunity to come to MIT, to conduct research in the Sloan Automotive Lab, and to learn and grow as a young engineer. Under his guidance, I learned the skills necessary to manage my time and projects and to think critically and solve the many problems that arise in experimental work. He not only emphasized the importance of graduate research, but also how to apply the knowledge learned here to be successful in industry.

My research would not have been possible without the support of the Aftertreatment Research Consortium. I learned a great deal from speaking with and presenting to the many industry representatives at our meetings.

I would like to give a special thanks to Dr. Kamp for being an incredible mentor and friend. His work ethic, passion for science, and wealth of knowledge have been an inspiration to me and have motivated me to constantly strive to do better work. Much of my research would not have been possible without his efforts.

I also want to thank Dr. Sappok for all of his support. He helped to make my transition to MIT and graduate research a smooth one through his guidance and his availability to help with any issue. I constantly borrowed from his experience and expertise in order to complete my research objectives.

My research would not have been possible with all of the help of the fantastic Sloan personnel. Thane DeWitt and Raymond Phan constantly went above and beyond to keep the lab running even in the midst of renovations and make sure our experimental setups were in working order. Janet Sabio was always behind the scenes making sure we had everything we needed. Their knowledge and expertise were invaluable and their company made the lab a pleasant workplace.

To my lab mates, Nick Custer, Paul Folino, Michael Arnold, Yosuke Obuchi, Yuesen Wang, Claudio Marciano, Amanda Hamlet, and Vicky Lee, thank you for making my time in the lab particularly enjoyable. With your help and friendship, my experience was infinitely more productive and memorable.

I would also like to thank the many people I have met at MIT. I have made some lifelong friends and have been able to work together on some incredible projects that have defined my experience at MIT.

Finally, I would like to thank my family. I never imagined I would be able to attend MIT and could not have done it without their love and support. This has been a once in a lifetime experience and it would not have been possible without all of your sacrifices.

(This page intentionally left blank)

CONTENTS

LIST OF FIGURES

LIST OF TABLES

(Page intentionally left blank)

NOMENCLATURE

AFR – Air/Fuel Ratio
CI – Compression Ignition
CO – Carbon Monoxide
CPSI – Cells Per Square Inch
CR – Compression Ratio
DPF – Diesel Particulate Filter
ER – Expansion Ratio
ESEM – Environmental Scanning Electron Microscopy
FIB – Focused Ion Beam
HC – Hydrocarbon
IC – Internal Combustion
ICE – Internal Combustion Engine
NO_x – Nitrogen Oxides
PM – Particulate Matter
SCR – Selective Catalytic Reduction
SI – Spark Ignition
SV – Space Velocity
TDC – Top Dead Center
TEM – Transmission Electron Microscope
X-Ray CT – X-Ray Computed Tomography
ZDDP – Zinc Dialkyldithiophosphates

(Page intentionally left blank)

1.   INTRODUCTION

The diesel engine is a reciprocating internal combustion (IC) engine that is used widely in transportation and power generation. The engine generates power through the combustion of an air and fuel mixture that drives a piston producing mechanical work. The diesel engine differs from a typical spark ignition engine in that the air is compressed to a high pressure and temperature and the diesel fuel is then injected, evaporated, and auto-ignited as opposed to the ignition energy being delivered from a spark plug. [1]

The diesel engine is extremely successful because it is a highly efficient power plant. Its high efficiency comes from the high compression ratios that it allows and low engine speeds. There is no concern for knock due to the injection scheme which is a typical concern for high compression in spark ignition (SI) engines. This higher efficiency also results in a lower CO2 output compared to gasoline engines but it has a lower specific output. These result in diesel engines being more effective for larger scale marine, highway, and power generation uses.

One major downside to diesel engines is the generation of a high amount of particulate matter or PM. This PM is a combination of carbon soot from locally rich regions of combustion and a metallic incombustible ash from lubricant additives. Both of these are hazardous to human health and can cause significant health issues. As a result, aftertreatment systems are used to collect and prevent these emissions. One of the major aftertreatment systems used and is the focus of this work is the diesel particulate filter (DPF) which is a porous ceramic honeycomb filter with filtration efficiencies up to 99%. The filter traps the soot and ash in its porous structure and allows the clean exhaust gasses to pass through. The collection of soot and ash, however, has a negative effect on filter performance and pressure drop and can also decrease the life of the filter. This increase in pressure drop can also decrease the efficiency and fuel economy of the system as well as increase operating and maintenance costs. There is a significant need to understand the deposition mechanisms, properties, and effects of this PM at both a macroscale level and a microscale level to increase filter performance and lifetime. The focus of this work will be a combination of micro and macro scale experiments and analysis to better understand the range of effects on the DPF.

1.1. Diesel Engines

The diesel engine was first created by Rudolph Diesel in 1892 and he subsequently built his prototype compression ignition engine in 1897. As mentioned, the primary difference between an SI engine and CI engine is the method of ignition of the fuel. This type of reciprocating internal combustion engine utilizes the high pressure compressed air and accurately timed fuel injection to produce combustion and release the energy required to create usable mechanical work. [1]

During the intake stroke, air is pulled at near atmospheric pressure into the cylinder through the motion of the piston. The intake valve then closes and the engine goes through the compression stroke. This is an area of significant difference with a typical SI engine since CI engines have typical compression ratios (CR) in the range of 12 − 24 compared to 8 − 12 in SI engines. The equation for thermal efficiency of an engine is shown below and is a function of CR assuming CR is equal to expansion ratio (ER). [1]

$$\eta = 1 - \left(\frac{1}{CR^{(\gamma-1)}} \right)$$

Thus, the higher compression ratio of the CI engine results in a higher thermal efficiency. CI engines can reach cylinder pressures as high as 40-50 bar and temperatures up to 800 - 1000⁰C during this compression stroke. Prior to the completion of the compression stroke at top dead center (TDC), atomized liquid fuel is injected into the cylinder at high pressure. This liquid fuel becomes entrained in the air and creates a combustible air-fuel mixture. The high temperature and pressure of the cylinder after the compression stroke ignites the mixture and the release of energy creates the work in the expansion stroke to drive the crankshaft. This work also drives the required pumping to push air out during the exhaust stroke and in during the next intake stroke. [1]

Another major difference between SI and CI engines is the method by which load is modulated or restricted. In a typical SI engine, the intake air is throttled using a valve. SI engines determine the amount of fuel to be injected based on the amount of throttled intake air comes in and a target

air/fuel ratio (AFR). CI engines, however, are not throttled and modulate their load purely through the amount of fuel injected. CI engines typically run very lean and so are not as sensitive to small changes in AFR as SI engines since they do not run at stoichiometric. These differences lead to some advantages and disadvantages compared to SI engines. [1]

1.1.1. Diesel Engine Advantages

There are several distinct advantages of diesel engines compared to traditional SI engines as a result of the differences mentioned above. The most obvious and significant advantage is the higher efficiency of the engine which leads to better fuel economy and decreased greenhouse gas emissions. Because of the relative simplicity of the diesel engine and lack of knock concerns, there is also increased durability, reliability, and lower maintenance costs. The unthrottled operation of the diesel engine also results in decreased pumping losses which results in higher efficiency. All of these combined improvements translate to a $20 - 40\%$ in fuel economy when compared to a similar output SI engine. [1]

Another benefit of the lean engine operation is the minimal amount of unburnt fuel remaining in the cylinder after each burn cycle. This results in lower hydrocarbon (HC) emissions which have negative impacts on human health. The higher AFR also greatly reduces the amount of carbon monoxide emissions (CO) which are directly related due to the high availability of oxygen for complete combustion. [3]

The heat release from diesel engines occurs at a faster rate and earlier in the combustion process which results in much higher torque at low speeds than SI engines. This operation at low speeds has distinct advantages. Frictional losses are reduced since they are speed dependent and lower operating speed also increases the reliability of the system and allows for larger engines. The heat losses also decrease with size which means that the diesel engine scales very well. This means that the diesel engine is an effective means of power generation for a wide range of applications. [1]

1.2. Diesel Engine Emissions

As mentioned before, one of the disadvantages of diesel engines are some of the emissions that are created. The two primary emissions of concern with diesel engines are nitrogen oxides (NO_x) and PM. NO_x emissions are generated at high temperatures and pressures where oxygen can react with relatively stable N_2 molecules. This means that NO_x generation is higher than in a similar power SI engine because of the diesel engine's higher CR. PM or carbonaceous soot, on the other hand, is a result of the fuel injection and mixing differences of a direct injection system like a diesel engine. While the full cylinder volume contains a very lean mixture of air and fuel, the effect of injecting atomized liquid fuel into the cylinder just before ignition is that there is locally a very heterogeneous mixture. Locally rich regions of air and fuel do not fully oxidize and creates this soot or ash if the local region includes lubricant. Finding methods for improved fuel air mixing is a large area for mitigation of PM generation but one main method to decrease soot generation is to increase cylinder temperatures. Higher cylinder temperatures lead to more complete oxidation of the carbon soot particles even after the initial burn phase. Unfortunately, as mentioned above, this leads to an increase in NO_x generation which brings about the NO_x/PM tradeoff in diesel engines. It is difficult to decrease the generation of one without impacting the other. There are several system options in place to reduce diesel emissions which will be discussed later. [3]

There are significant human health hazards associated with diesel exhaust emissions that necessitate reductions in emissions. Longer term exposure to the contaminants in diesel exhaust can lead to the development of lung cancer. Even short term exposure to the fine particles lead to eye, nose, throat, and lung irritation. It can also cause coughs, headaches, and nausea. These emissions also can cause the development and aggravation of chronic respiratory symptoms or asthma. The formation and release of NO_x is also a primary constituent of acid rain. [4]

As a result of PM and NO_x generation as well as CO and HC and all of their associated health effects, there are regulations in place limiting the amount of each emission type that can be created. Over time, these restrictions have become increasingly more stringent, signaling a need for increased public safety as well as motivation for engineering improvement.
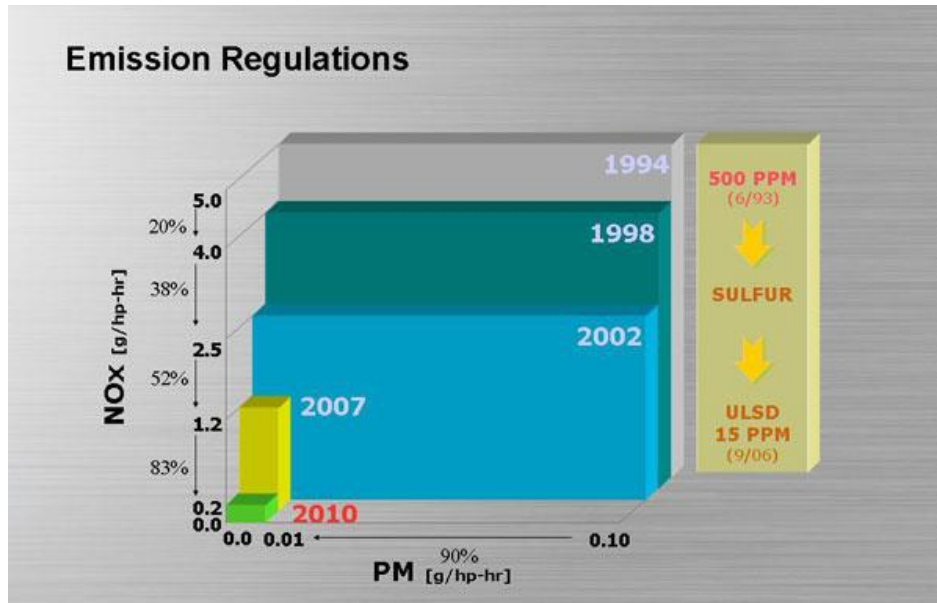
Figure 1.1: EPA NOx and PM Standards Over Time

As shown in Figure 1.1, there has been order of magnitude reductions in allowable PM and NO_x emissions over the past two decades requiring new systems and methods for emission reductions. [6]

1.2.1. Emission Reduction Methods

There are several different types of diesel emission reduction systems that have been implemented in order to keep up with the increasingly stringent emission standards. The first involves changes in engine configuration, operating conditions, and control strategy. These typically result in either running in inefficient modes to reduce emissions and causing a fuel economy penalty or still run into the standard PM/NO_x tradeoff. Other methods of reducing engine emissions are achieved through the use of aftertreatment systems. These are systems downstream of the engine with the purpose of either treating or removing the emissions so they are not harmful upon release. Because HC and CO emissions are comparatively low in a diesel engine, the main focus is the reduction of NO_x and PM.

One method of treating NO_x emissions is through the use of a selective catalytic reduction (SCR) system. This is a system by which the reduction of NO_x emissions occurs through mixture with

nitrogen compounds such as ammonia or urea in the presence of typically platinum catalysts. Through several chemical processes, the NOx compounds are converted with the nitrogen compounds into nitrogen gas and water. The benefit is that the NO_x is removed from the exhaust stream however the nitrogen compound is consumed in the process. This requires both an expensive aftertreatment system as well as an ammonia or urea tank that needs to be refilled. Another system that is used is a lean NO_x trap which is a porous material called zeolite that absorbs NOx. The zeolite can absorb a finite amount of these emissions before it must be treated which also creates an expensive and repetitive process. [7]

The primary method of controlling PM emissions is through the use of a DPF. As briefly mentioned, this is a porous ceramic honeycomb filter that traps particulate emissions while allowing gaseous exhaust to escape through the filter. This method is highly effective since it has filtration efficiencies of up to 99%. However, as more PM is captured within the filter, the restriction to exhaust flow increases which increases the backpressure on the engine and reduces fuel economy. To clear out the buildup of carbon soot, the filter is periodically regenerated at high temperature to burn off the soot into CO_2. While the soot is removed, a small amount of metallic ash particles derived from the lubricant additives remain in the filter. Over the life of the filter and after many regeneration cycles, the impact of this metallic ash becomes significant. There has been a large effort to understand the many effects that this ash has on filter performance as well as how to mitigate these effects. The next section will investigate some of the current knowledge while the main body of this work will seek to further understand these mechanisms.

(Page intentionally left blank)

2.   DIESEL PARTICULATE FILTERS

The primary method used for soot capture and oxidation in order to meet PM emission regulations is the DPF. Commercial DPFs were first used in in 1985 on Mercedes cars equipped with a 3.0 L turbocharged IDI engine sold in California. After initial technical issues plagued the use of the DPF, continuing development and stringent particle emission reduction requirements of $80 - 90\%$ promoted widespread adoption of the DPF. This includes both on and off highway as well as light and heavy duty vehicles. As a relatively simple system to implement, the DPF has also has been used as a retro fit solution on many vehicles. [8]

2.1.   DPF Fundamentals

As a result of years of development iterations, the most common type of DPF is a ceramic, honeycomb, wall flow monolith filter due to its cost and high filtration efficiency. The honeycomb structure is made of an extruded porous ceramic with flow channels open at the inlet and outlet. A wall flow filter is one where every other inlet channel is plugged and the opposite outlet channels are plugged. This geometry forces the exhaust gasses to filter through the porous channel walls down the length of the filter where particles can be trapped. An example of this structure is shown below in Figure 2.1.
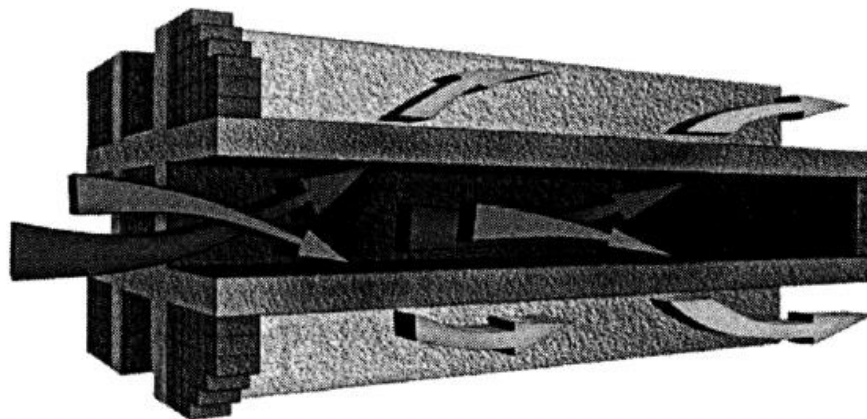
Figure 2.1: Flow Direction of Wall Flow Monolith DPF

As a result, the porous structure is the critical filtration medium and is a tightly controlled part of the manufacturing process. As PM starts to build up in the pores and ultimately on top of the channel wall surface, the filtration efficiency increases due to it acting as an additional filter medium. This results in filtration efficiencies up to 99%. [9] However, this accumulation increases the flow restriction within the pores of the filter and increases the thickness of the porous medium that it must flow through. This increase in back pressure results in a decrease in fuel economy. [10] The PM that is trapped in the filter is a combination of mostly carbonaceous soot and a small amount of metallic ash derived from lubricant additives. The soot comprises about 99% of the PM matter by mass. [11] To reduce back pressure and reopen space in the filter to capture PM, the combustible PM is oxidized at elevated temperatures of $150 - 650^{\circ}\text{C}$ depending on the chemistry and presence of catalysts. This oxidation, called filter regeneration, either happens periodically or continuously depending on the operating conditions and method of regeneration. Typically, regeneration requires fuel to create the additional heat which is another fuel penalty for the DPF.

Due to the short life span and relative uniformity of the soot within the filter compared with the ash particles, the properties and effects of soot accumulation are fairly well understood. Over a wide range of engine operating conditions, the soot layer porosity remains around 90% with a permeability around $2 \times 10^{-14} \text{ m}^2$. [12] The lubricant derived ash, made of a variety of chemistries and remaining in the filter until physically cleaned, have varied properties and effects on the filter which will be discussed further.

2.2. Lubricant Derived Ash

While lubricant derived ash only accounts for 1% of the engine out PM, its continued existence after regeneration cycles means that it can have an increasing effect on filter performance relative to soot. As early as 30,000 miles or the equivalent engine run hours, 50% of the filter PM can consist of ash particles. [13] The ash portion of filter PM over the life of the filter is shown below in Figure 2.2: **Portion of Filter PM Consisting of Ash Over Filter Life**Figure 2.2.
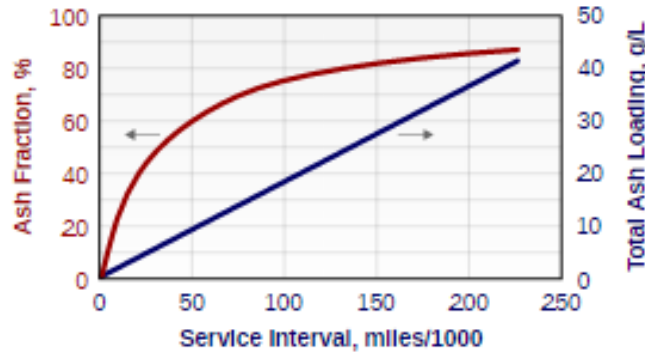
Figure 2.2: Portion of Filter PM Consisting of Ash Over Filter Life

As ash is deposited in the filter, it builds as both a cake layer on top of the channel walls and as a plug at the end of the channel. This is seen below in Figure 2.3. As soot is continually regenerated, the ash cake layer becomes the new filtration medium and the soot layer builds on top of the ash. The following sections will discuss the sources of this ash and the different types of chemistries. It will also discuss the performance effect of the ash on the DPF over the life of the filter and as a result of ash chemistry.

Figure 2.3: Typical Location of Ash Deposition Within a DPF

2.2.1. Ash Sources and Chemistries

As stated, the deposition of ash particles within the filter can be detrimental to both the filter performance as well as the operating life of the filter. Over time, the presence of ash requires a cleaning of the filter to remove the volume of ash and reduce pressure drop. A filter can only be successfully cleaned a small number of times before the DPF must be replaced. This process is both time consuming and expensive for the filter owners motivating methods for decreased ash impact on the filters. The accumulated ash is derived from a number of sources including engine wear particles and metals found in the fuel. The primary source of ash comes from the engine oil. During operation, a small amount of engine oil lining the cylinder walls is combusted with the fuel air mixture. The organic components are oxidized either in the cylinder or further downstream but the metallic compounds from the additives are left as ash particles. A typical diesel engine oil consists of 75-83% organic base oil, 5-8% viscosity modifier, and 12-18% lubricant additives from which the ash is derived. The inorganic portion that generates the ash constitutes 1% of the oil. [14] The base oil acts as the primary lubricating ingredient due to its beneficial lubrication qualities such as viscosity, viscosity index, pour point, and oxidation resistance. [15] The oil is also the carrier for the lubricant additives which are used improve the performance and lifetime of the oil. These additives are also the primary source of metallic ash particles in the DPF. The main types of additives used are detergents, dispersants, and Zinc Dialkyldithiophosphates (ZDDP).

Detergents are used as lubricant additives to work as a corrosion inhibitor. Detergents contain metal salts and an organic component, typically calcium and magnesium, combined with a base, usually carbonate. The basic components of the detergents act to neutralize the acidic components of combustion/oxidation byproducts. After neutralization, the organic portion of the detergent suspends the byproducts within the lubricant. These two acts of neutralizing acidic components and suspension of byproducts help to reduce engine rust and corrosion as well as particle buildup. The metal components are the primary constituents of ash PM in both sulfate and oxide form after combustion. There is a tradeoff between limited use of detergents to decrease ash generation while requiring them to limit engine corrosion. [15]

The second set of additives in diesel lubrication is the dispersants. These act in a similar manner as the secondary effect of detergents in that they are added to suspend insoluble wear and corrosion particles within the lubricant to prevent particle buildup. While the detergents have some small dispersant properties, dedicated dispersants are required to adequately keep the engine components clean. Another important difference between the two is that the dispersants do not contain any metal elements which means that they do not contribute to the ash formation of concern.

The final additive group is ZDDP which has been used in many types of lubricants primarily as a low cost anti-wear agent. When small surface imperfections on lubricated sliding surfaces penetrate the lubrication film creating higher temperature metal-to-metal contact, the ZDDP acts to reduce the contact to prevent wear or surface welding. ZDDP is composed of sulfur, phosphorous, and zinc which are all undesirable emissions components. The presence of zinc also contributes to the formation of ash particles within the DPF. While magnesium and calcium compounds make up the large majority of ash constituents, the presence of even a small amount of zinc can have important impacts on ash properties due to its different morphology and lower melting temperature. [16]

2.3.   Ash Effects on DPF Performance

There has been a large effort to understand the effect of lubricant ash on DPF performance and flow restriction. While the general effects are fairly well understood, the many mechanisms and variables by which this deposition and restriction occur are yet to be characterized accurately.

Figure 2.4 shows an example of a typical pressure drop curve of a cordierite DPF across the lifetime of the filter before being cleaned. There are three main regimes of ash deposition that are apparent in the pressure drop curve shown with corresponding renderings to demonstrate the location of ash in each regime. The first critical regime is the deep bed filtration regime. This occurs within the first ~5 g/L of ash where early ash particles are deposited within the pores of the filter. These ash particles begin to block critical flow pathways and cause a sharp increase in pressure drop. This is a particularly important regime because only a few percent of the ash that

will accumulate in the filter over time can account for up to 50% of the total ash loaded pressure drop. The deposition of these first ash particles set the baseline by which the rest of the pressure drop builds off of. This means that there is an opportunity to reduce the pressure drop over the life of the filter through potential control of the deposition in the earliest portion of the filter life.

After the surface pores have been mostly filled in the deep bed filtration regime, the transition regime begins. This is when the initial steep slope starts to round off and flatten out as new particles are no longer being deposited into the filter but instead start to stack onto previously deposited ash particles. Under continued loading, the filter transitions to the final stage which is the ash cake layer regime. In this regime, new particles never reach the filter material and only stack up in a cake layer of increasing thickness. The ash cake layer effectively becomes the new filtration material. The pressure drop increases slowly as a result of the increased thickness of the ash cake layer which provides new flow restriction. Ash in this regime also gets pushed to the end of the inlet channels and starts to build up as an ash plug. As this plug increases in length towards the front of the filter, there is a decrease in available filter area for exhaust gasses to pass through. This decrease in filter area in conjunction with the building cake layer leads to the increased slope halfway through the cake layer regime. [4]
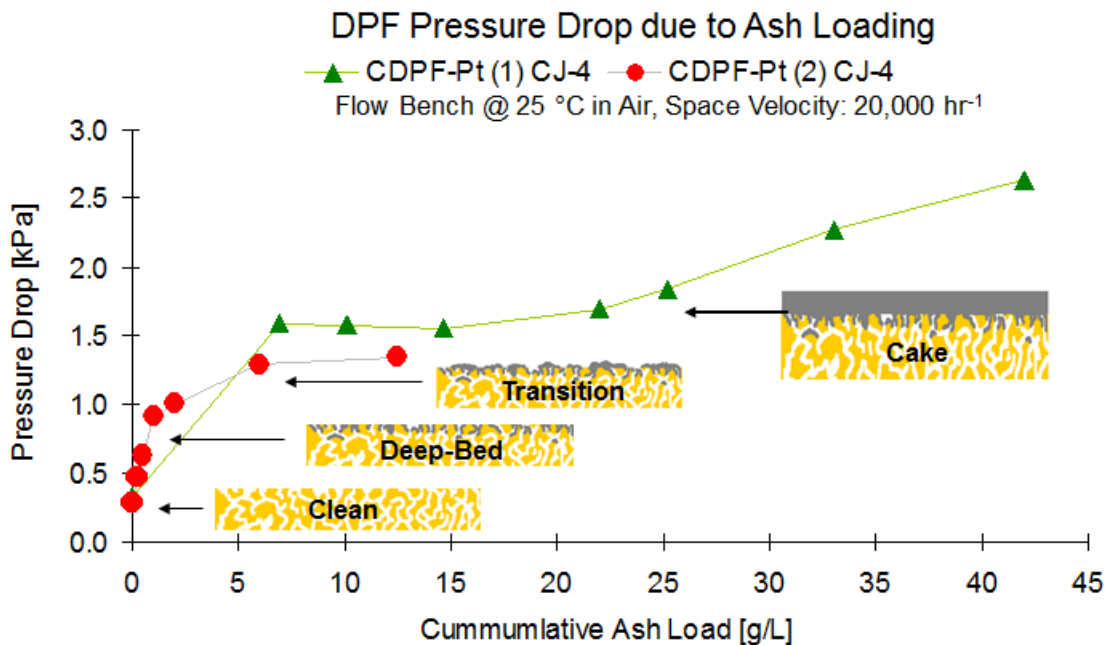
Figure 2.4: Stages of Ash Deposition in DPF and Effect on Pressure Drop in [4]

27

While Figure 2.4 demonstrates just the ash effect on filter performance, the existence of ash has an important effect on filter response to soot loading. As shown in Figure 2.5, with no ash in the filter, the response to soot loading follows a similar trend to the filter response to ash loading. There is a clear steep increase under a small amount of soot load followed by a longer linear increase in pressure drop. The two main differences are that the transition point happens at a very low amount of soot load of under 0.5 g/L and that the magnitude of pressure drop increase is up to six times higher for the same loaded mass of PM. This is due to the smaller particle size of ash that allows for better penetration into the pores of the filter as well as the lower permeability of soot cake layer compared to ash cake layer. [17]
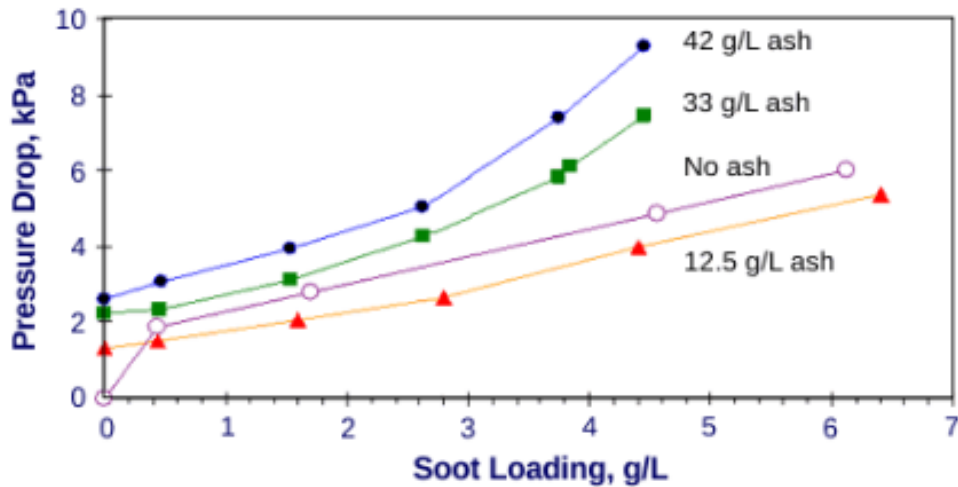
Figure 2.5: Effect of Ash Loading on Soot Loaded Pressure Drop Increase in [17]

Once an ash cake layer has built up in the filter, the net pressure drop increase due to the 12.5 g/L of ash and the soot related pressure drop is actually lower than with the soot by itself. This is a result of the small, more permeable ash cake layer acts as the filter substrate for the soot particles preventing the deep bed regime of soot loading from occurring. Instead, the effect of the deep bed regime of the ash is much lower than that of the soot which makes the net effect more beneficial. This only lasts to an extent as can be seen by the 33 g/L ash loading which has a higher pressure drop than all instances of the no-ash soot loading cycle. In this case, the total effect of the deep bed regime and thick cake layer of the ash is larger than the effect of the deep

bed filtration of the soot that is prevented. This demonstrates another instance in which the deep bed filtration regime is an important section of the filter life to control to decrease the effect of soot loading on pressure drop. The high ash loaded cases also show a similar increase in the slope of pressure drop with additional loading due to the reduction in filter flow area from the increase in plug length.

2.3.1. Lubricant Additive Chemistry Effects

Several additional ash loading experiments were done in [4] using a number of single additive lubricant formulations to determine the effect of ash chemistry on filter performance. The results of this study are shown below in Figure 2.6. Each type of ash exhibits pressure drop trends following the same types of regimes as talked about previously. The different additive types show a range of effects in each regime. In the initial deep bed filtration regime, the calcium and magnesium ash loaded filters have the highest initial pressure drop rise. The magnesium filter changes to the transition regime much earlier for an initial cake layer regime with almost half of the pressure drop. From there, the magnesium loaded filter has an extremely flat pressure drop trend implying a very high permeability cake layer. The calcium loaded filter, on the other hand has the highest cake layer slope of any of the filters. The zinc loaded filter has the smallest difference between the deep bed and cake layer regimes. The CJ-4 ash loaded filter, which contains components of each individual type of ash, is in the middle of the spectrum for both regimes. This also seems to show the additive effects of each of the different types of ash chemistries.

At the end of the ash loading process, several ash layer properties were measured including packing density and porosity. Each ash type had an extremely high porosity around 90% showing how loosely packed and porous the ash particles are. The packing density variation was slightly higher between $0.19 - 0.30$ g/cm^3. The presence of calcium ash appears to drive up the packing density of the ash. One limitation of this type of analysis is that the ash properties can only be measured in a post mortem analysis after the final loading point. This removes the possibility of additional loading and only provides one data point for ash properties as a function of ash load and run time.

29
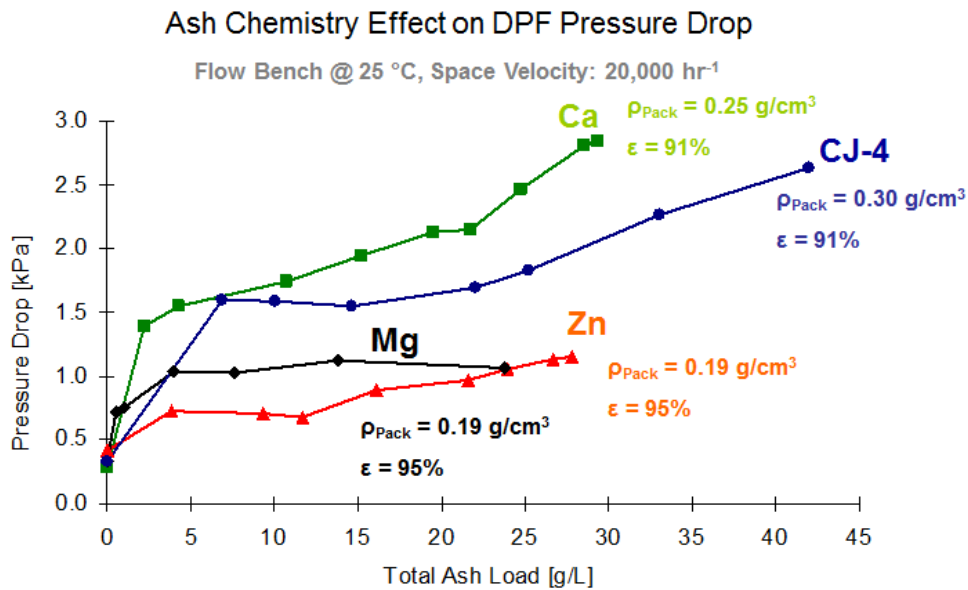
Figure 2.6: Pressure Drop Trends of Several DPFs Loaded with Single Additive Ash Chemistries

During the post mortem analysis, many other properties of the ash particles can be determined through the use of advanced diagnostics. Using a transmission electron microscope (TEM), the morphology of the ash can be found providing insights into the variation of measured pressure drop.
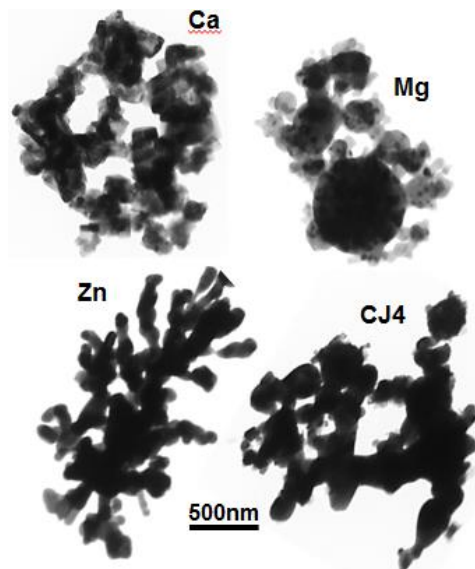
Figure 2.7: Morphology Variation Due to Ash Chemistry

As can be seen in Figure 2.7, there are distinct differences in the morphology for each type of ash. The calcium ash consists of small spherical particles around 100 nm in diameter. These particles appear tightly bound together which is consistent with the higher packing density and higher pressure drop. Tightly bound particles are less likely to be moved by the exhaust gasses and only provide small openings for flow which could drive up the pressure drop as seen above. The magnesium ash consists of large, loosely bound spherical particles. The large particles allow for much larger, more permeable flow pathways which are consistent with the lower cake layer pressure drop and a faster deep bed regime. The zinc particles are the most distinct looking particles of the group with a defined, branch-like structure. The lower melting temperature and greater surface area of the particles make the zinc ash more susceptible to partial melting and sintering during local high temperature events from soot oxidation. The CJ-4 ash particles appear to have some combined features of each of the other types of ash which is also consistent with its relative pressure drop trends. Large spherical magnesium components and smaller more branched zinc components are also apparent.

In addition to the other ash properties such as packing density and porosity, it is important to understand the permeability or flow restriction of ash as well as the effect of lubricant additive type and morphology on it. Due to the relative difficulty of measuring permeability from a small ash sample compared to density or porosity, efforts were made by Yujun Wang in [19] to estimate both the ash cake layer permeability and composite wall and deep bed ash permeability from the pressure drop trends above. This is done by separating the pressure drop curve into two component slopes with the slope of the deep bed filtration regime representing the composite wall permeability and the cake layer slope representing the ash permeability. The components of pressure drop not directly from flow through a porous medium is calculated and removed. What is left is used in the Darcy equation to calculate permeability. The results are shown below in Table 2.1.

Table 2.1: Results of Permeability Estimations in [19]

Lubricant	Ash Permeability (m^2)	Wall Permeability (m^2)
Ca	1.67 x 10^{-14}	4.56 x 10^{-14}
Zn	8.56 x 10^{-14}	10.5 x 10^{-14}
Mg	57.4 x 10^{-14}	5.82 x 10^{-14}
Ca + Zn	4.46 x 10^{-14}	3.75 x 10^{-14}
MG + Zn	4.80 x 10^{-14}	9.35 x 10^{-14}
CJ-4	11.1 x 10^{-14}	4.98 x 10^{-14}

The values of ash permeability shown above span over an order of magnitude and are within a similar range of other previous permeability measurements. There are significant limitations with this method due to the low resolution of pressure drop data with respect to ash loading and the need to remove multiple components of pressure drop contribution to be left with the pressure drop due to the permeable material. The properties of the ash used in the calculation only represent one moment across the life of the filter. A large focus of this work is to develop additional, more accurate methods to measure and calculate permeability in order to use this key parameter as a method to determine the effectiveness of other ash parameters in reducing pressure drop.

(Page intentionally left blank)

3.   EXPERIMENTAL SETUP AND APPROACH

As a result of the detrimental impact on DPF performance of the lubricant derived ash particles, there is significant value in understanding both the deposition mechanisms of the ash into the filter as well as the corresponding flow properties. In order to better understand these effects and properties, a number of experiments are designed.

3.1.   Compressed Ash Permeability Experiment

Previous experiments have shown the large scale DPF performance decrease as a result of ash accumulation but there is difficulty in separating properties such as ash packing density, lubricant additive type, and DPF geometry and understanding how each contributes to system pressure drop. Additionally, the many drivers of the pressure drop make it difficult to measure individual permeability of the materials present. The goal of this experiment is to remove both the ash and filter material from the large honeycomb structure of the DPF and set up a 1D flow regime so that the permeability can be measured accurately.

An accurate permeability measurement over a range of ash chemistries and packing density allows for significant improvements in modelling accuracy and justifications for new additive formulations to reduce pressure drop.

3.1.1. Experiment Design

As mentioned in Section 2.3, there are two main regimes where the addition of ash and soot particles to the filter can increase pressure drop. In the deep bed filtration regime, the ash particles are embedded within the porous flow network of the DPF and block critical flow pathways. This results in the sharp pressure drop increase with a relatively low amount of ash that is seen repeatedly. The second regime is the ash cake layer regime where the ash builds up in a somewhat uniform cake layer that replaces the porous ceramic as the primary filter substrate for the soot particles. The additional pressure drop increase is due to the permeability of the ash cake layer and the geometry of the cake layer as it grows. While the cake layer growth is well

understood, there is significant interest in measuring the permeability with high accuracy so as to improve modeling and see what variables impact cake layer permeability.

For a DPF in field use, there are several major components that result in the total system pressure drop. They are shown in Table 3.1.

Table 3.1: Contributions to DPF Pressure Drop

Pressure Drop Term	% Contribution
Contraction Losses (Inlet)	<3%
Frictional Losses Along Inlet Channel Walls	5-30%
Frictional Losses Through Wall, Ash, and Soot	50-90%
Frictional Losses Along Outer Channel Walls	~5%
Expansion Losses (Outlet)	<3%

As much as half of the total pressure drop can be a result of the geometry of the exhaust ducting and filter geometry. In order to calculate an accurate permeability for the ash cake layer, the pressure drop contributions due to contraction losses, expansion losses, and frictional losses along the channel walls need to be removed by the system design and is achieved through the use of a cordierite wafer.

As mentioned in Section 2.3.1, the permeability calculations from the full DPF pressure drop data attempt to account for each of these pressure drop contributions. However, the density of the ash cake layer is taken to be constant and is only measured at the final loading level. This assumption does not take into consideration the variation of ash cake layer density over time due to changes in temperature, flow rate, or high temperature events. It also does not consider the local variation of packing density within the filter. To overcome this, the ash tested in this experiment is packed across a range of typical packing densities found within a DPF.

3.1.2. System Design

Based on the goals and requirements listed above, a flow bench system is designed to measure the pressure drop across the porous medium so that permeability can be accurately calculated. The flow bench schematic is shown in Figure 3.1.
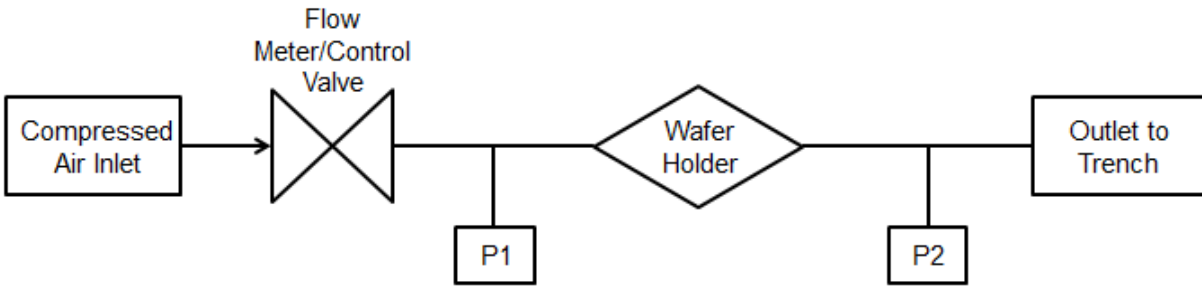
Figure 3.1: Schematic of Flow Bench

This simple system allows for accurate air flow control and pressure measurement in a sealed system while requiring a special holder for the wafer and ash. The system is designed to be mounted in a vertical orientation so loose ash is not disturbed by gravity or falls to one side of the flow. The density is then controlled by measuring a precise mass of ash and compressing it to a constant volume using a specially designed packing tool and using the known diameter of the tube. This idea is demonstrated in Figure 3.2.
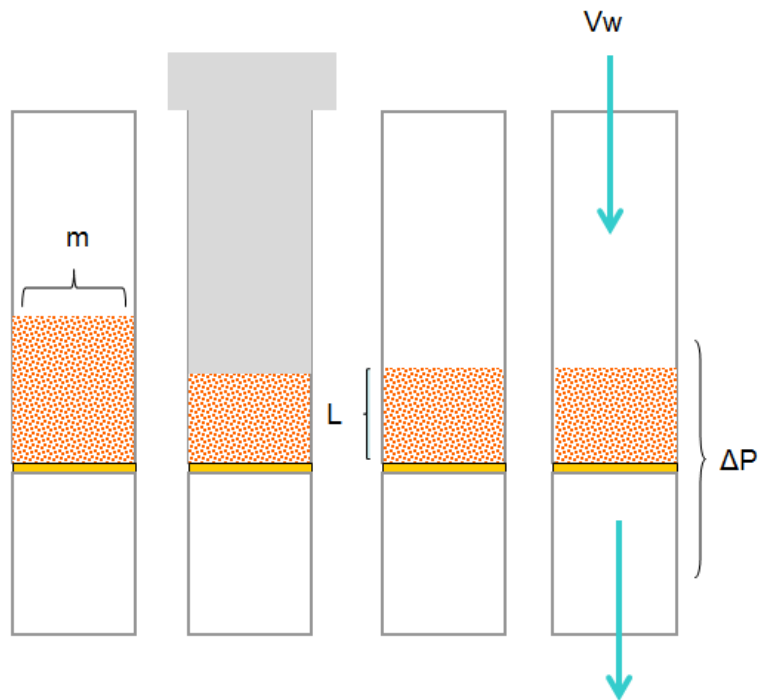
Figure 3.2: Ash Loading Process for Accurate Density

This process of controlling the packing density through a controlled volume allows for a density accuracy of ± 0.005 g/cm^3.

To accurately represent the flow conditions in a DPF in field use, the wall velocity through the wafer must be equal to the average wall velocity through the channel walls of the DPF. Space velocity (SV) is a term used to describe the normalized volume flow rate through a given volume of filter. The equation is described below.

$$Space\ Velocity = \frac{Volume\ Flow\ Rate}{Filter\ Volume}$$

A typical range of space velocities in field use is from $0 - 100{,}000$ 1/hr. This encompasses conditions varying from idle to wide open throttle. Since a wafer is only defined by its wall velocity and not a space velocity, the space velocity must be converted. For the typical range of space velocities in a filter, the range of line velocities through the channel walls is calculated. The manufacturer's specifications for a cylindrical DPF provide the diameter (D), length (l), wall thickness (t), and cells per unit area on the front face (CPA). The number of cells is typically provided in cells per square inch (CPSI).They also provide the length of the plug section on the inlet and outlet channels (l_p). Using these specifications, the equation for number of channels is shown below (N_c).

$$N_c = \pi \frac{D^2}{4} * CPSI$$

For a typical 5.66" x 6", 300 CPSI filter, this equates to about 5030 total channels including both inlet and outlet channels. To avoid double counting walls, only the inlet channels or half of all channels contribute to flow surface. Next, the surface area for each channel (A_c) needs to be found. This is shown below.

$$A_c = 2 * \left(\frac{1}{\sqrt{CPSI}} - t\right) * (l - l_p)$$

Multiplying by the number of channels, the total flow area of a typical filter is about 4.5 m^2. Using the outer dimensions of the filter, a typical filter volume is 2.47 L. With the space velocity, filter volume (V), and total wall area (A), the wall velocity (V$_w$) can be found. This is shown in the equation below.

$$V_w = \frac{SV * V}{A}$$

Using this conversion from space velocity to wall velocity, an approximate wall velocity range is from 0 to 3.5 cm/s. This is the critical value to match between filter sizes when choosing a volume flow rate for the wafer sample. Next, the diameter of the tube for the flow bench needs to be chosen. There is a relatively small amount of each type of ash available from the previously loaded lab filters. In order to ensure enough ash is available to provide an adequately thick cake layer, a tube diameter of 0.62" is chosen. Using this diameter, a test range of volume flow rate from 0 to 400 standard cubic centimeters per minute (SCCM) is found. An Omega mass flow controller, FMA-2620A, is chosen to accurately control the flow rate through the system.

A specialized wafer holder is designed in order to hold the brittle ceramic wafer without breaking. It is also required to prevent air from escaping the system for accurate pressure measurements and to retain the ash cake layer. The design for the holder is shown in Figure 3.3.
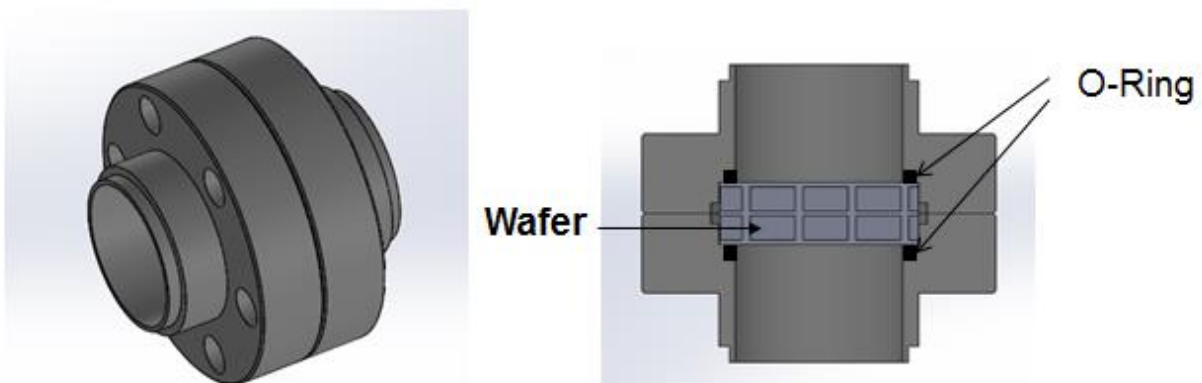
Figure 3.3: Design of Wafer Holder

The wafer holder as shown uses a wafer cut from a full, 200 CPSI, uncoated DPF with a wall thickness of 450 μm. A two channel, three wall thickness was chosen for its additional structural support to avoid fracture of the cordierite. The two flanges are bolted together with a gasket to prevent leaks. The wafer is held between two compliant O-rings in the flange to direct all flow through the wafer material instead of around. To prevent the air from flowing out the channels on the sides and to provide more structural support where the wafer will be stressed from the O-rings, the channel openings are covered with an epoxy. A prepared wafer sample and one with the ash cake layer are shown below in Figure 3.4.

Figure 3.4: The Stages of Wafer Sample Preparation and Loading

As seen above, a small wafer section is cut roughly from a section of DPF and sanded to the correct size. Using increasingly fine grit sandpaper, the wafer section is brought to 0.75" diameter and the perpendicular channel walls are ground flat for a smooth flow surface. The epoxy is then applied to the outer channel openings and is allowed to dry. After drying, the epoxy is then also sanded to the correct diameter to fit within the wafer holder. With the wafer assembled in the wafer holder and the flow bench assembled, the pressure drop experiments can be run.

3.1.3. Test Matrix and Procedure

As mentioned, the test setup is used to measure the pressure drop over an ash cake layer that is held up by a cordierite wafer. The two main variables being tested are the lubricant additive chemistry or the chemical makeup of the ash and the controlled packing density of the ash cake layer. The test matrix is shown in Table 3.2.

Table 3.2: Test Matrix for Ash Cake Layer Permeability Experiment

Ash Sample Type	Volume Flow Rate (SCCM)	Equivalent Space Velocities (1/hr)	Packing Density (g/cm^3)
Field Ash Active	0 - 400	0 - 100,000	0.15 - 0.75
Field Ash w/ Soot	0 - 400	0 - 100,000	0.15 - 0.75
CJ4 Active	0 - 400	0 - 100,000	0.15 - 0.75
CJ4 Passive	0 - 400	0 - 100,000	0.15 - 0.75
Base + Ca	0 - 400	0 - 100,000	0.15 - 0.75
Base + Zn/Mg	0 - 400	0 - 100,000	0.15 - 0.75
Base + Mg	0 - 400	0 - 100,000	0.15 - 0.75
Base + Zn	0 - 400	0 - 100,000	0.15 - 0.75

Typical packing densities of ash cake layers found in lab and field samples are in the range of values of 0.25 to 0.6 g/cm^3 with it going as high as 1 g/cm^3 for highly sintered agglomerates. This experiment is primarily concerned with ash particles packed into a cake rather than a fully sintered region. For that reason, a range of packing densities of 0.15 - 0.75 g/cm^3 is chosen to understand the full range of typical values and to see the trends near the extremes of typical packing densities.

The ash samples used in this experiment are derived from both lab and field generated samples. The field ash samples are from CJ4 oils in highway use that contain 1% ash by mass. The field ash came with a small amount of soot which is oxidized to create the pure ash field sample. The lab generated samples are all derived from the loading experiments described in [5]. The additive contents of the oils used in lab filter loading are described below.

Table 3.3: Lubricant Elemental Composition Used in the Experiments Described in [5]

Lubricant	B (ppm)	Ca (ppm)	Fe (ppm)	Mg (ppm)	P (ppm)	Zn (ppm)	S (ppm)	Mo (ppm)
CJ-4	586	1388	2	355	985	1226	3200	77
Base Oil + Ca	3	2928	1	5	2	<1	609	<1
Base Oil + ZDDP	1	<1	<1	<1	2530	2612	6901	<1

Experimental Procedure

Once the clean wafer is mounted into the holder and assembled in the flow bench, the flow rate is swept from 0 to 400 SSCM at a rate of 100 SCCM/min while the pressure is measured. This allows for the calculation of the wafer permeability as well as the normalization to find the pressure drop increase strictly due to the addition of the ash cake layer. Next, the sample section is removed and a precise mass of ash is added to the wafer giving an expected packing density of 0.15 g/cm^3. The ash is then moved around until it is approximately evenly distributed to avoid regions of varying density but overall nominal packing density. A specially made piston with a slip fit with the tube is used to compact the ash to the correct volume. The piston has a seat matching with the top of the tube to prevent additional, unwanted travel. With the ash loaded, the holder is reattached to the flow bench where the flow sweep and pressure measurement procedures are repeated.

For all additional ash loading steps, the preceding ash cake layer is loosened and disturbed before adding the new ash to prevent stratification of the cake layer of different properties and to also to prevent localized density variation. The new mass of ash is then added to increase the packing density to the next step. The ash is then mixed until approximately evenly distributed and packed again. This procedure is repeated for each value of packing density and the full test matrix.

3.2. Initial Pore Build-up and Lubricant Chemistry Experiment

As seen in Section 2.3, the general long term effect of ash buildup on a DPF is fairly well understood. While the previous experiment described the need for a better understanding of ash cake layer properties in the later regime of ash loading, there is also much interest in understanding the initial deep bed filtration regime. Both regimes account for roughly half of the total pressure drop of the DPF and as such are both critical pieces. The deep bed filtration regime also takes place within the first 5 g/L of loading which means that a very small amount of ash has a significant impact on pressure drop.

Previous experiments only capture a very low resolution and small portion of the deep bed filtration regime with one to two pressure drop points. This prevents an accurate measurement of

the slope and shape of the pressure drop trend at low ash loading. The tolerance for ash loading measurement is also as high as 2 g/L which means that previous data does not fully represent this important phenomenon or the specific trends. One of the goals for this experiment is to develop the methods to measure with much higher accuracy the amount of ash loading within the filter even at low levels. This allows for a much higher resolution of pressure drop with respect to ash loading. Additionally, the chemistry of the lubricant additives has shown to have a significant impact on both the morphology of the ash being deposited as well as its ultimate pressure drop. This experiment will also investigate the differences in initial ash buildup from different lubricant additive types.

3.2.1. System Design and Setup

As mentioned, the goal for this experiment is to understand the effects of lubricant additive chemistry on overall DPF pressure drop with high resolution in the deep bed filtration regime. To gather this type of data in a field setting or in a lab with an engine used for the ash loading of the filter, this would take approximately 600 hours or 20,000 miles of equivalent highway usage per filter. Additional time would also be required for regeneration, pressure drop testing, and other analysis. Because this is a significant amount of time, especially for any loading past the deep bed filtration regime, an accelerated ash loading system is used to generate ash particles in conjunction with a Yanmar diesel engine to provide soot. This system has been used repeatedly for the rapid aging of DPFs and has been shown to repeatably generate and deposit ash and soot particles in the DPF.

The system used at MIT is a very versatile system since the primary exhaust gases are generated by a diesel burner rather than an engine. This allows for much greater control over fuel injection rates and flow rates since it is not RPM limited. In addition, the large downstream counterflow heat exchanger allows for wide temperature control from 200 °C through regeneration temperatures as high as 700 °C. The ash producing oil is atomized and injected into the combustion chamber where it is burned and enters the exhaust stream. This independent oil injection system is the key component in accelerated ash loading because the injection rate is independently controlled. This method of injecting oil also generates more representative ash

compared to doping the fuel with additional oil because it allows for a burn in an air rich region and because the atomized oil has less of a tendency to bind together in an incombustible mass of metallic compounds. A schematic of the accelerated ash loading system is shown below in Figure 3.5.
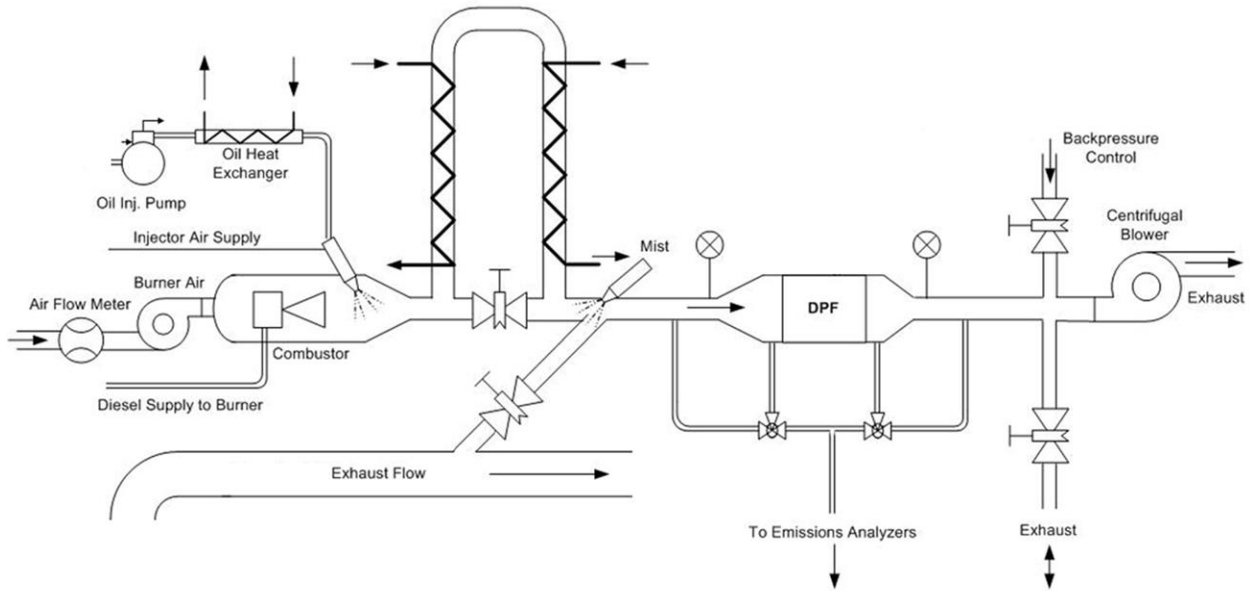
Figure 3.5: MIT Accelerated Ash Loading System Schematic

As see in the above schematic, air is drawn through the system from a large centrifugal vacuum pump at the end of the system. The flow rate is measured at the inlet to the system before passing through the burner where it is mixed with diesel fuel and combusted to create the exhaust gases. The oil is then atomized and injected with a small amount of air to facilitate combustion and ash particulate generation. The system temperature is then regulated through the heat exchanger and gate valve before passing through the DPF. Inlet and outlet temperature and pressure are measured across the DPF to ensure the correct operating conditions and measure filter performance as a function of loading. Before the pump, a secondary inlet valve allows for ambient air to be pulled in to the system to reduce the exhaust temperature to below the acceptable level for the pump. The exhaust gases are then passed into an exhaust trench where it is removed. The burner operating conditions are shown in Table 3.4.

Table 3.4: Accelerated Ash Loading System Operating Conditions

	Operating Range	Experiment Setting
Fuel Consumption	1.5 - 7.6 L/h	5.7 L/h
Oil Consumption	0.94 - 9.4 mL/min	4.1 mL/min
Injection Pressure	700 - 1400 kPa	1250 kPa
Air Flow	500 - 1700 SLPM	1400 SLPM
DPF Inlet Temperature	200 - 800°C	300 - 650°C

In addition to the diesel burner and oil injector, a small diesel generator is connected just downstream of the heat exchanger. Because the diesel burner uses a constant flow fuel nozzle and constant speed internal pump, the fuel burns at a fairly constant AFR with only a small amount of soot. The diesel generator is used to generate much larger amounts of soot in a controlled manner. The inlet from the burner is closed off and the diesel engine is run to generate a large amount of soot for when soot loading is necessary. Soot loading is typically used on new filters to characterize initial filter performance or to look at the effects of high soot loading on a filter with an ash layer already generated from the accelerated aging system. The specs of the diesel engine are shown in Table 3.5.

Table 3.5: Specifications of Diesel Engine for Soot Loading

Model	Yanmar L100V
Displacement	0.435 L
Output	5000 W @ 3600 RPM
Soot Generation Rate	2.5 g/hr
Air Flow	1050 SLPM
DPF Inlet Temperature	260°C

One of the major necessary changes from the previous system for this experiment is the method of holding and weighing the DPF for accurate measurement of mass and ash loading. Prior experiments encased the DPF in an insulated stainless steel clamshell can with expanding and reducing cones on the ends to connect to the three inch diameter pipe system. This was used for creating a tight seal, providing significant insulation of the DPF from the ambient air, and to allow for clamped connections to the larger system. However, this system weighs about 10 kg which requires the use of a larger scale with 0.2 g resolution. The filter itself only weighs 1.2 kg which can fit on a lower mass, higher resolution scale. While the filter can technically be removed, it would require significant disassembly and reassembly time as well as a repetition of the expansion process for the insulation.

A new filter holder is designed to allow for the easy removal of the DPF for mass measurement on a 0.01 g resolution scale with a maximum allowable mass of 2 kg. The new filter must also prevent air leakage and provide insulation to keep temperature variation within the filter to below 50ºC. The proposed design consists of clamping the inlet and outlet faces of the DPF between inlet and outlet connecting cones with threaded rods. The cones have a sealing surface with a gasket in contact with the outer ring of the DPF to prevent leakage. The design is presented in Figure 3.6.
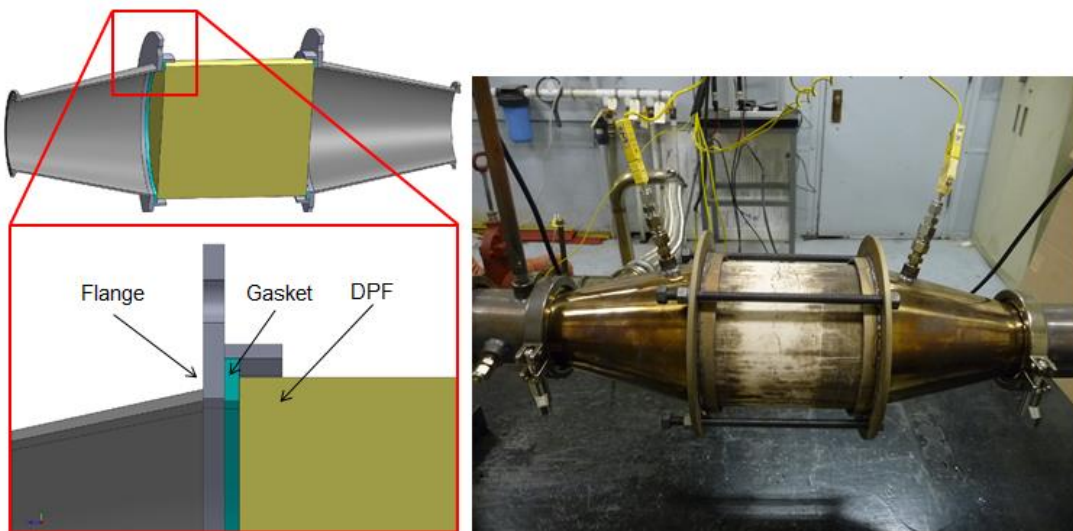

Figure 3.6: Design of New Filter Holder for Quick Removal

The sets of threaded rods are tightened to provide the seal between the DPF faces, gaskets, and flange surfaces. Two sets of gaskets are used for different portions of the experimental process. For all high temperature conditions, stiff high temperature graphite gaskets are used to prevent melting or degradation. During room temperature flow and pressure drop tests, a more compliant rubber gasket is used to provide a better seal during the critical pressure measurements.

As currently shown, the filter does not have adequate insulation and can have radial temperature variation of up to 100°C. A flexible casing with high temperature insulation is placed over the outside of the holder with a quick clamp for easy removal. With the additional casing, the radial temperature variation remains below 50°C.

Under the new design, the filter is rigidly mounted to the rest of the system and is susceptible to damage from vibrations in the system, particularly from the engine. As a result, additional vibration isolation components including damping engine mounts and softer flexible pipe between the engine and larger system are added. These prevent the filter from seeing any significant vibrational loads and prevent the brittle cordierite from cracking.

3.2.2. Test Plan

Using the accelerated ash loading system and filter holder described in section 3.2.2, a test plan is developed to repeatably measure the effects of deep bed filtration of ash on filter performance. As mentioned in section 2.3.1, there are significant differences in both the ash morphology and impact on system pressure drop as a result of various lubricant additive chemistries. The most notable is the stark contrast between the calcium and magnesium single additive lubricants. In order to understand the performance differences at higher resolution and the mechanisms by which they occur, this experiment looks at ash generated from two oils that meet the criteria of a CJ4 oil but are high in either calcium or magnesium content. These satisfy current regulatory requirements but aim to match the characteristics exhibited in the single additive formulations. The basic oil additive formulation is shown in Table 3.6.

Table 3.6: Lubricant Additive Formulation for Experimental CJ4 Oils

Lubricant Type	Ca [ppm]	Mg [ppm]	P [ppm]
High Ca	2480	<1	800
High Mg	<1	2050	800

Due to the significant time investment required to ash load a filter and measure performance, there is very little data on the repeatability of pressure drop response to ash load taken under identical conditions. Since this experiment focuses on only the early deep bed filtration regime, it is possible to measure the repeatability of the response under low ash load which still can account for up to 50% of the total response. This is done through the loading of three filters under identical process for each oil formulation for a total of six filters. The specifications of the filters used are shown in Table 3.7.

Table 3.7: Filter Specifications for Ash Loading Experiment

Substrate	Cordierite
Catalyst	Pt
Dimensions	D5.66" x 6"
	(D14.4 x 15.2 cm)
Cell Density	200 cells/in^2 (31 cells/cm^2)
Wall Thickness	0.012"
	(0.03mm)
Volume	2.47 L
Mass	1.3 kg

The six filters are normalized by initially soot loading and measuring pressure drop to compare performance without loading ash. Each filter is loaded to 6 g/L of soot in 2 g/L increments and pressure drop is measured at each point. Pressure drop is measured by pulling room temperature air through the filter from $0 - 100$ SCFM while inlet and outlet pressure are measured. After the clean and soot loaded pressure drops are measured for normalization, the soot is then regenerated so that clean filters are left.

The first filter is loaded at 300°C with ash from the high magnesium oil for 45 minutes to an estimated 0.33 g/L. The oil injection is then turned off and the temperature is increased to 650°C for 30 minutes to oxidize any soot generated during ash loading. Once the filter is cooled, the pressure drop increase due to the additional ash is measured and the filter is weighed to accurately measure the increase in ash load. The pressure drop of the filter is measured at room temperature by a stepwise process. Starting at zero flow, the pressure drop is measured for 2 minutes at each point followed by an increase in blower frequency of 5 Hz to the next flow level. Depending on the pressure drop of the filter, this is repeated to the full blower power which results in a final flow rate of about 100,000 hr^{-1}. This process is repeated every 0.33 g/L up to 3 g/L which provides a much higher resolution of pressure drop. This is done for each of the three magnesium loaded filters. After the magnesium filters are loaded, the accelerated ash loading system is taken apart and cleaned thoroughly to remove any residual ash and soot particles that remain attached along any part of the flow system. This is done to prevent any contamination of the magnesium ash in the second set of filters. After the system is cleaned and reassembled, the final three filters are loaded with the same procedure using the high calcium oil.

After each filter is loaded to 3 g/L, one filter of each type then undergoes post mortem analysis. This includes breaking open the filter for image analysis using environmental electron scanning microscopy (ESEM) and focused ion beam milling (FIB). These high resolution imaging tools give insight into the location, size, shape, and deposition mechanisms of the ash within the filter. Image data used in conjunction with the pressure drop trends provide a more complete picture of the effects of ash on DPF performance and the differences between the additive formulations.

(Page intentionally left blank)

4. RESULTS

4.1. Compressed Ash Permeability Experiment

The following results describe the pressure drop and permeability measurements from the experiment described in Section 3.1. As mentioned, the ash samples are taken from both field and lab generated samples using a variety of additive formulations. For each set of ash cake layer pressure drop measurements, the values are compared against the clean wafer on which the ash is deposited. The clean wafer also provides a baseline permeability value for comparison.

4.1.1. Pressure Drop Results and Repeatability

The purpose of the designed vertical flow bench is to accurately measure the pressure drop over the compressed ash cake layer and cordierite DPF wafer. This pressure drop and the known geometry of the ash cake layer and flow conditions is used to then calculate permeability through the porous ash medium.
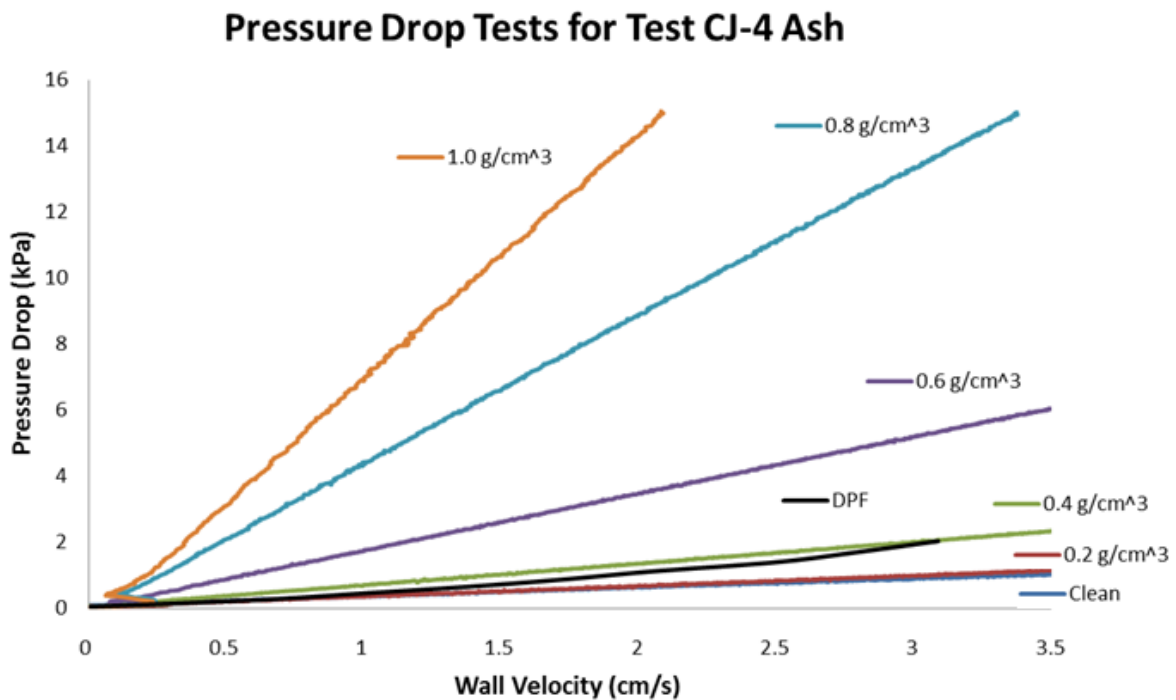

Figure 4.1: Pressure Drop vs Flow Rate for a Test Ash for Repeatability

Figure 4.1 demonstrates one such example of the pressure drop trends across a range of wall velocities of 0 – 3.5 cm/s or volume flow rates from 0 – 400 SCCM. This is the equivalent wall velocity seen in a filter with typical space velocities of 0 – 100,000 1/hr. The pressure drop trend at each packing density is linear compared to the pressure drop vs flow rate for a full size DPF which is quadratic. A sample DPF pressure drop curve for a clean filter is also shown. It is slightly higher across the range of flow range than the wafer and increases at higher flow rates. The quadratic pressure drop trend for a full side filter is not just due to the permeability of the porous medium but also the other flow restriction effects mentioned earlier such as channel friction and expansion losses that are flow dependent. The linear trend of this data demonstrates the improvements made in this wafer setup.

Figure 4.1 also shows the significant increase in pressure drop due to the increased packing density. At packing densities below 0.3 g/cm^3, and even with an artificially thick cake layer of up to 20x typical thicknesses, the pressure drop addition due to ash is not significant compared to the pressure drop due to the filter material. Above 0.3 g/cm^3, the pressure drop rapidly increases beyond the peak pressure drop of even the highest ash or soot loaded filters. The increase of pressure drop of over an order of magnitude demonstrates the significant and nonlinear result of increased packing density. The increase in the packing density of the ash also relates to the decrease in the porosity (ε) through the theoretical packing density of the ash compounds.

$$\varepsilon = 1 - \frac{\rho_{ash}}{\rho_{theoretical}}$$

Taking the slope of each of these curves, which will be used to calculate permeability, this effect is clearly shown in Figure 4.2. Also included is the slope vs packing density data for 5 additional runs to find the repeatability of the system using a sample of CJ4 ash.
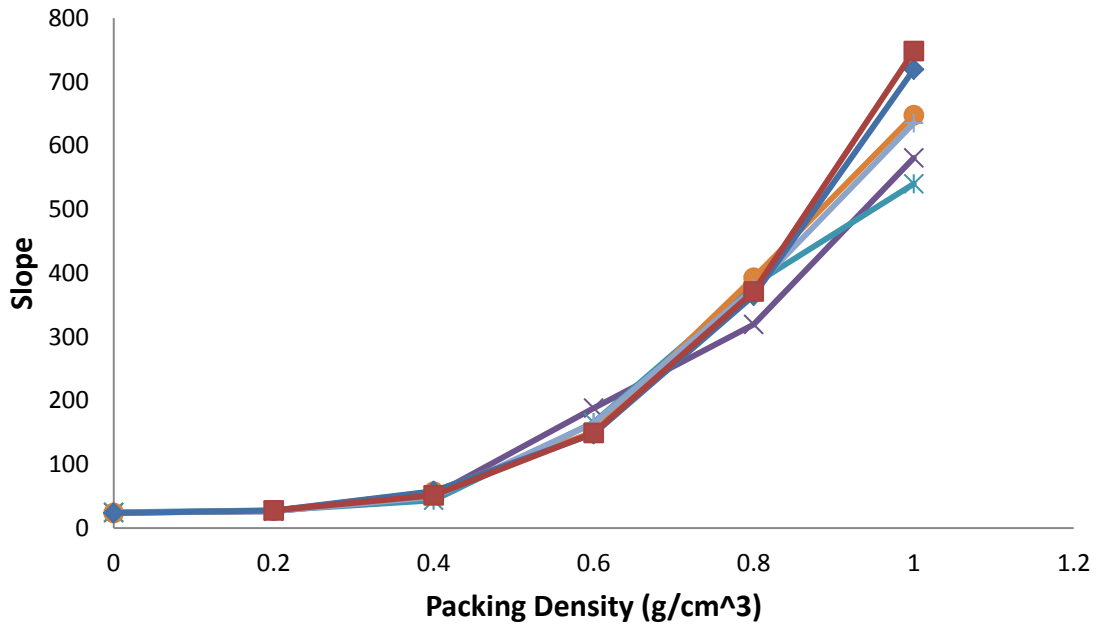
Figure 4.2: Slope of Pressure Drop vs Flow Rate Curves at Each Packing Density for 6 Repeatability Runs
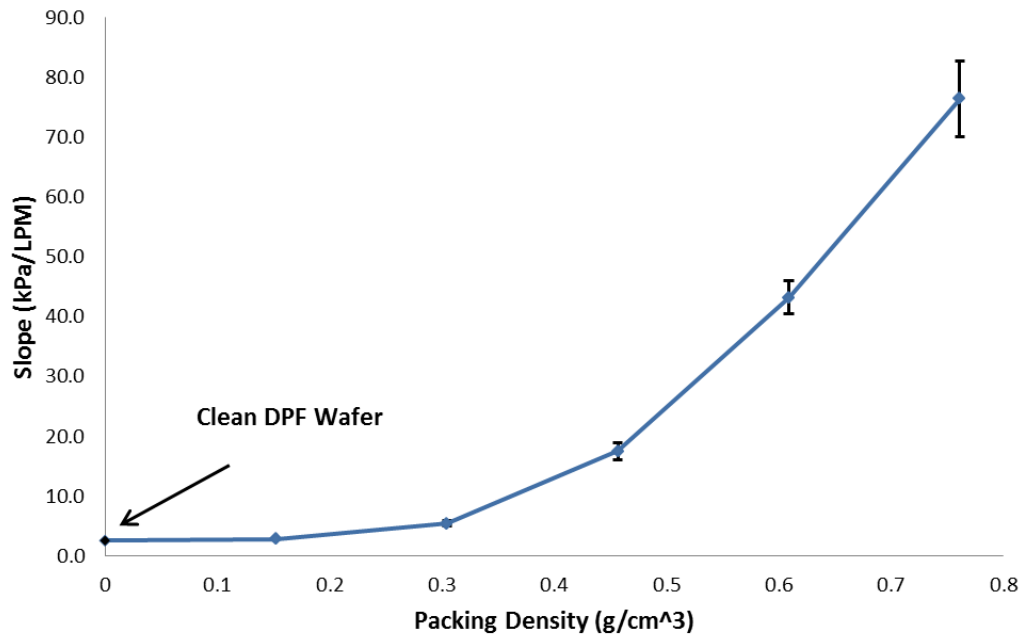

Figure 4.3: 95% Confidence Interval of Slopes over 6 Repeatability Runs

Figure 4.2 and Figure 4.3 demonstrate the strong repeatability of the system, especially at lower packing densities. Below 0.45 g/cm³, the average standard deviation is around 2% of the pressure drop value. At higher packing densities, the system becomes slightly less repeatable with an increase of the average standard deviation to 8% of the nominal value. One likely reason for the decrease in repeatability at the higher packing densities is the larger mass of ash used to create the cake layer. When the ash is mixed and loosened before packing, it must be spread extremely evenly. If during compression, there is an uneven distribution of ash, local regions of varied packing density can be created. This is more likely with higher packing densities. Localized regions of varied packing density could be responsible for the small variations in the measured pressure drop. The lower packing densities are much more representative of an ash cake layer seen in the field where a typical packing density varies from 0.15 to 0.6 g/cm³. Higher packing densities seen in the field are typically comprised of a partially sintered ash cake layer which the packed ash cake layer in this experiment will not capture the differences in properties.
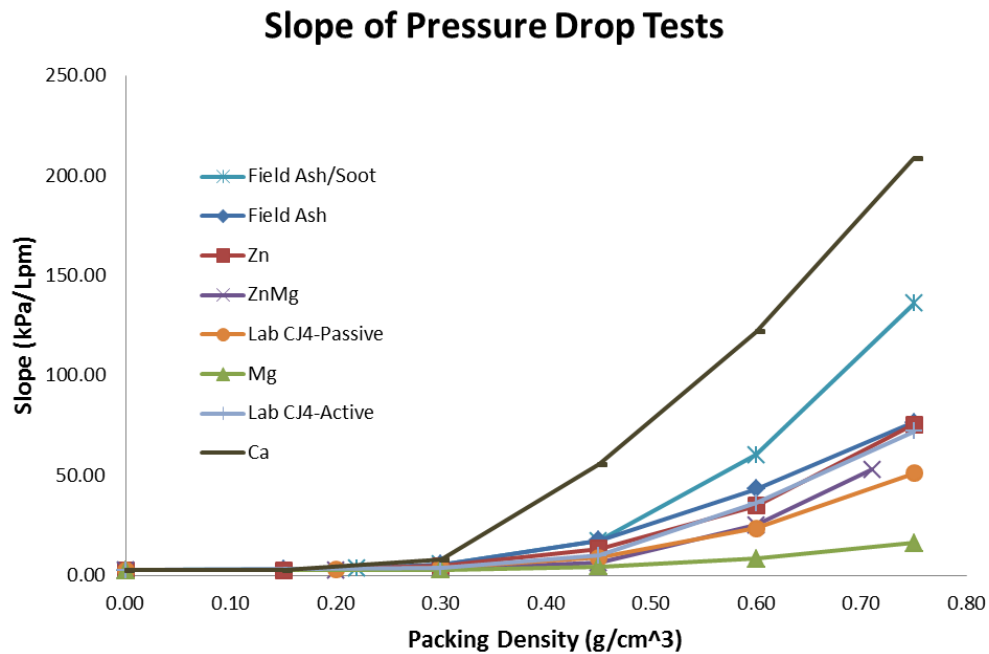

Figure 4.4: Pressure Drop Slopes vs Packing Density for Each Ash Type

After completing the system repeatability study using the large amount of test ash, multiple ash types from field and lab generated sources in the test matrix were measured using the same procedure. These ash samples were taken by removing the ash cake layer and plug section from a number of channels of the loaded filters. Due to the small amount of ash available and large amount of ash needed for the experiment, each sample could only be tested once while the repeatability of the test sample is used to determine the significance of any differences in pressure drop. In Figure 4.4, it is possible to see the significant impact of lubricant additive chemistry on the slope of pressure drop per unit flow rate. While the parabolic shape is consistent amongst all ash types, the magnitude difference is drastic. This is especially clear at the highest packing density where the maximum peak is for the lab generated calcium ash at 206 kPa/SLPM compared with the minimum for the lab generated magnesium ash at 13.7 kPa/SLPM. This also supports the previous data in section 2.3.1 that the difference in magnesium and calcium morphology contributes to a large difference in filter performance.

In order to find the permeability for each of these ash types and packing densities, the pressure drop data is offset by the pressure drop due to the clean wafer so that the measured pressure drop data is only a measure of the flow restriction across the ash cake layer. This pressure drop, in conjunction with the fixed geometry of the ash cake layer and known volume flow (Q) and viscosity (μ) of room temperature air are used to calculate the ash cake layer permeability (κ). This relationship is known as the Darcy equation and is shown below.

$$Q = \frac{\kappa * A * \Delta P}{\mu * L}$$

Permeability in this equation is a measure of the ability of a gas to penetrate through the porous medium. It is an intrinsic property of the material. The permeability is a function of both the porosity of the material as well as the 3D structure of the material. The Kozeny-Carman equation determines this 3D structure as a function of the mean particle diameter (D) as well as the sphericity of the particle (Φ) which is a measure of the area to volume ratio of the particle or how close to spherical it is. The value for permeability using this correlation is shown below.

$$\kappa = f(\epsilon) * g(particle) \qquad\qquad \kappa = \frac{\varepsilon^3}{(1-\varepsilon)^2} * \frac{D^2\Phi^2}{180}$$

Using the Darcy equation, the permeability for all ash types and packing densities are displayed below in Figure 4.5.
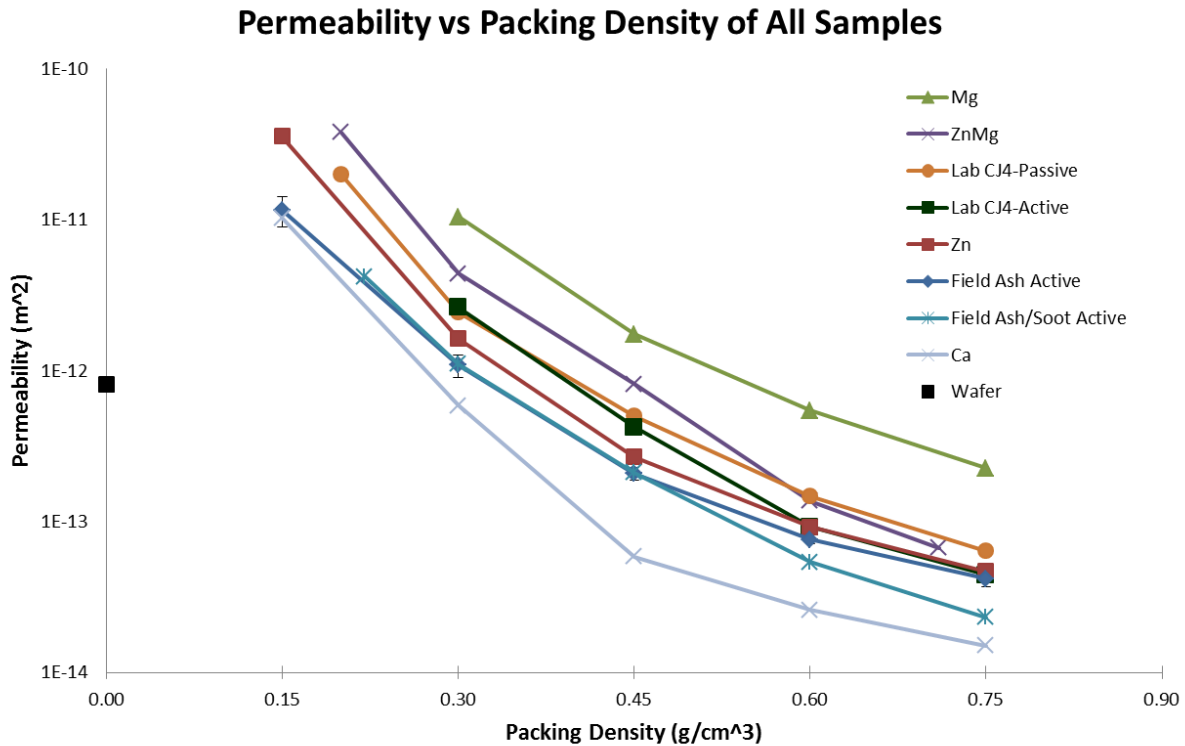
Figure 4.5: Permeability vs Packing Density for All Lab and Field Samples on Log Scale

As the wide range of slope values implies and as can be seen in Figure 4.5, the packing density has an extremely strong impact on the permeability of the ash cake layer. Across a typical range seen in the field, the ash cake layer permeability spans over two orders of magnitude emphasizing the importance of controlling this property of the cake layer to improve filter performance. These packing densities correspond to a porosity range of about $75 - 95\%$. The wafer itself was measured to have a permeability of 8.13 E-13 m^2. The permeability of the ash cake layer spans on either side of this measured wafer permeability which supports the trends seen in the full DPF pressure drop trends as a result of ash cake layer buildup.

One important comparison to make is the difference between lab generated ash and field generated ash. As seen in Figure 4.6, both lab samples have a higher permeability than the field samples. This is likely due to the tightly controlled procedures and temperatures of the accelerated ash loading system which generates a very uniform particle size and ash cake layer. Field generated ash samples can see many instances of highly variable flow from the engine exhaust as well as high temperature events. These high temperature events can come from the engine side as well as a non-uniform regeneration strategy. Local regions of high soot load during regeneration can result in local filter temperatures above the ash melting point and can cause non uniformity in particle size as well as sintering. These filters have shown evidence of these extreme temperature events and are a possible cause of the lower permeability of the field generated samples. A sample permeability curve using the Kozeny-Carman correlation using typical values for CJ-4 ash particle size and sphericity is also plotted. There is reasonable agreement the middle of the packing range but it has a slightly less dramatic effect at the extremes. The porosity effect accounts for the large change in permeability due to packing density/porosity while the ash particle properties mainly account for the vertical difference between ash types at a given packing density.
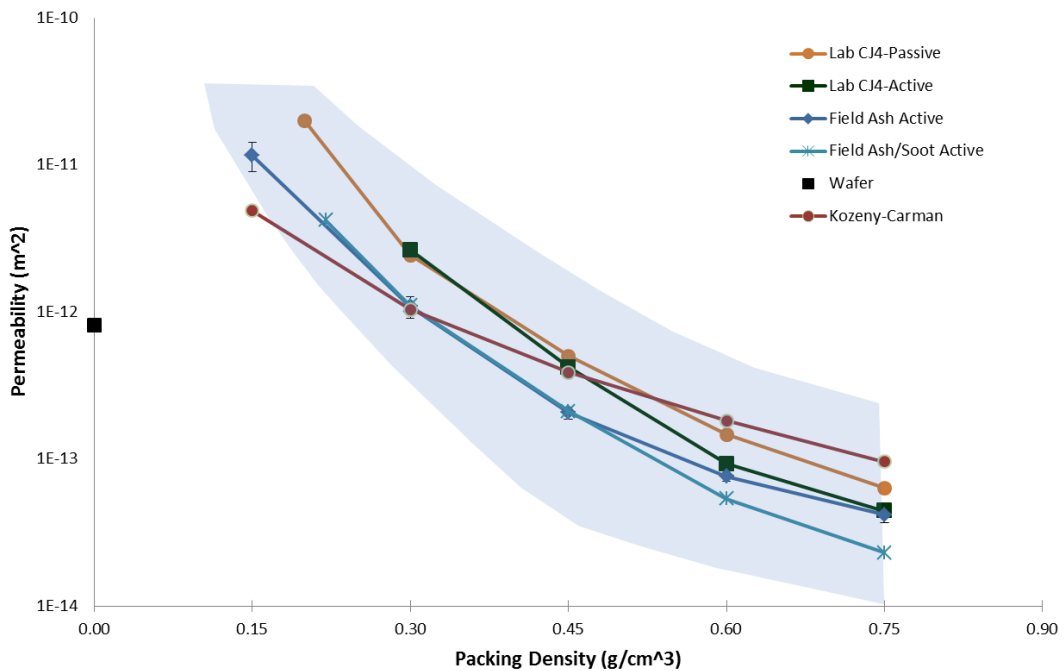

Figure 4.6: Comparison of Lab and Field Ash Permeability

The difference between the lab generated CJ4 ash under an active regeneration strategy compared to a passive regeneration strategy is also demonstrated in Figure 4.6. In this case, the passive regeneration actually means that it is continuously loaded at 600°C so that soot is continuously regenerated and does not built up in the filter. The resultant effect is that the ash particle size is smaller since soot oxidation has the effect of drawing smaller ash particles together to form larger particles and agglomerations. It is surprising that the permeability for the passive sample is higher since the particle size is smaller. It is possible that the difference in morphology allows for the packing to occur differently. However, the difference in permeability is small especially in the lower range of packing densities where the test method is more representative of the ash cake layer.
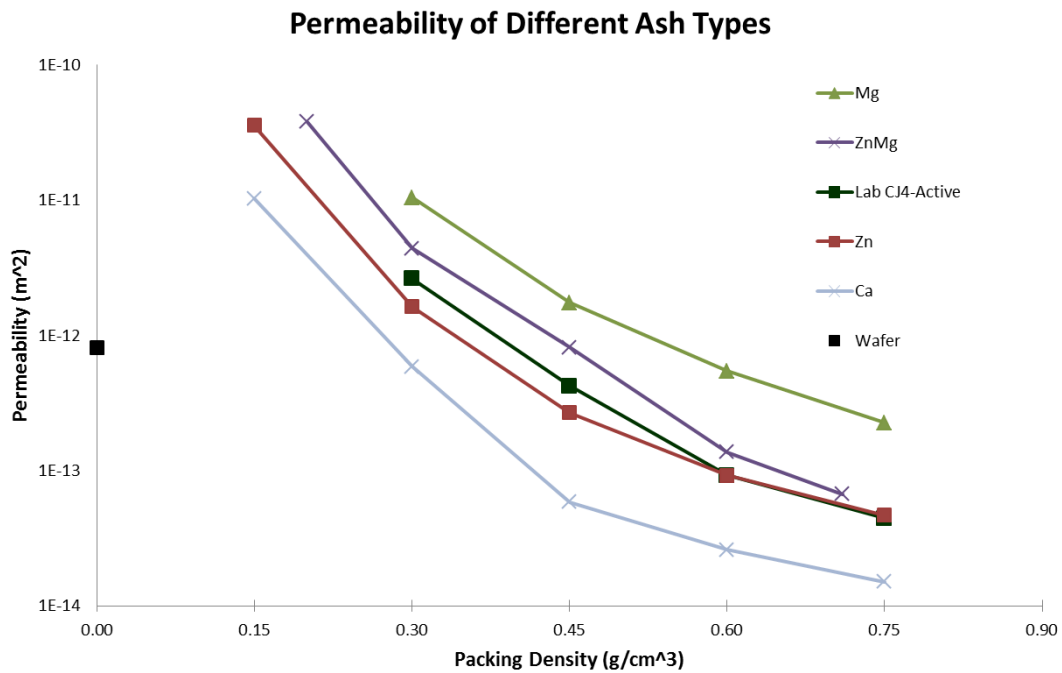

Figure 4.7: Comparison of Lab Generated Ash Permeability of Various Lubricant Additive Compositions

Shown in Figure 4.7 is a comparison of the permeability for each of the different lubricant additive formulations used in [5]. At any given packing density, the difference in permeability due to lubricant additives is significantly larger than the difference in lab vs field samples or

57

regeneration strategy. This emphasizes the importance of formulation as a way to control the mechanisms of ash deposition and filter performance. The clear separation of magnesium and calcium ash also stands out as they are consistently over an order of magnitude apart in permeability. This is likely due to the morphology of each of these ash chemistries.

Magnesium ash particles are typically large spherical particles that are loosely bound and allow for larger flow pathways between particles. Calcium ash is comprised of smaller, more tightly bound spherical particles that contain smaller flow pathways. Calcium particles also stick together more closely and prevent air flow. Zinc ash particles are significantly different than magnesium or calcium and form a more porous, branch-like structure. While not as open as magnesium particles, its branched structure can intertwine under higher packing densities resulting in a lower permeability. CJ4 ash, being comprised of a combination of the other ash types has a morphology that includes some of the properties of each of the other types. This results in a permeability that is in the middle of each of the individual types of ash. The CJ4 ash data as well as the Zn/Mg ash data both seem to show that the addition of magnesium particles has a significant impact on increasing the permeability of the ash in which it is introduced. This has strong implications for methods of improving oil formulations.
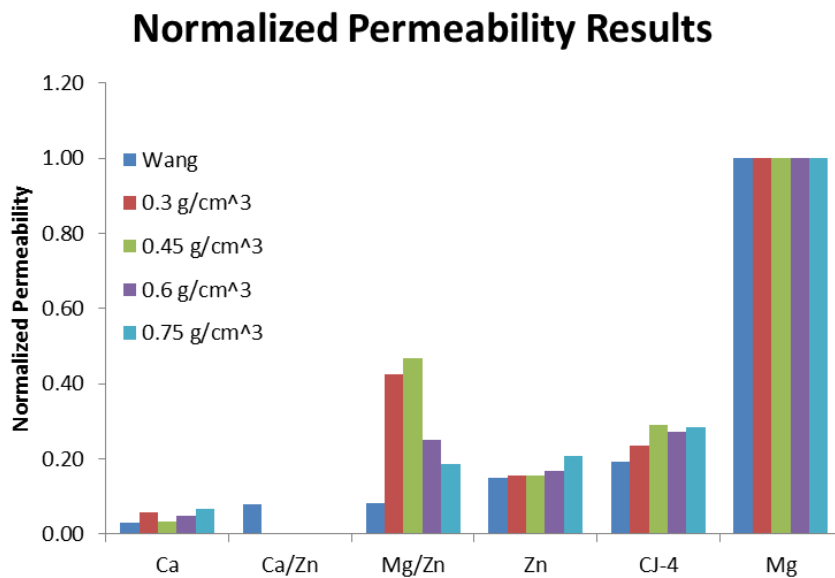

Figure 4.8: Relative Permeability Comparison Normalized to Magnesium At Each Packing Density

Figure 4.8 demonstrates the relative permeability of each of the different ash types. At each packing density, the permeability is normalized to the value of the magnesium ash. While the permeability itself varies significantly with packing density, there is very little variation with respect to each other with the exception of the Mg/Zn ash. In addition, the relative permeabilities from the previous work in [19] is also shown. These permeability values are derived from using the slope of the full DPF pressure drop curve and the single packing density at the end of the loading. The relative permeability of the single additive ash shows good agreement with that of the estimated permeability. In the case of the Ca/Zn sample, there was not enough ash remaining to complete a test of permeability vs packing density. This data shows that the relative effect of the additive chemistry on the permeability stays fairly constant even as the permeability changes due to the packing density.

4.2. Initial Pore Build-up and Lubricant Chemistry Experiment

The following section investigates the resulting filter pressure drop as a result of both high magnesium and high calcium ash loading within the deep bed filtration regime. There is also a strong focus on the repeatability of the system for use in future experiments. Finally, the micro scale images taken in the post mortem analysis help to provide an understanding of the deposition mechanisms and differences between the types of ash.

4.2.1. Pressure Drop Results

As mentioned in Section 3.2.2, the six filters used in the experiment were loaded with soot to 6 g/L with pressure drop measured in 2 g/L increments for normalization between filters and to test for faulty filters. Figure 4.9 demonstrates a sample set of pressure drop data for one of the filters at each level of initial soot loading. The pressure drop response is not linear due to the various portions of pressure drop not related to flow through the porous medium. This includes viscous friction in the channels as well as expansion and contraction losses at the inlet and outlets. This graph also shows the significant impact of soot loading on filter pressure drop. At 6 g/L of soot, the filter has up to 9 times the pressure drop of clean filter. While the data is measured at stepwise increments of flow rate, continuous pressure drop vs flow results can be gleaned from a

quadratic fit of the data. The data for different loading amounts can then be compared at the same flow rate to see the impact of just PM loading. From this graph alone, there is some indication of a higher pressure drop response in just the first 2 g/L.
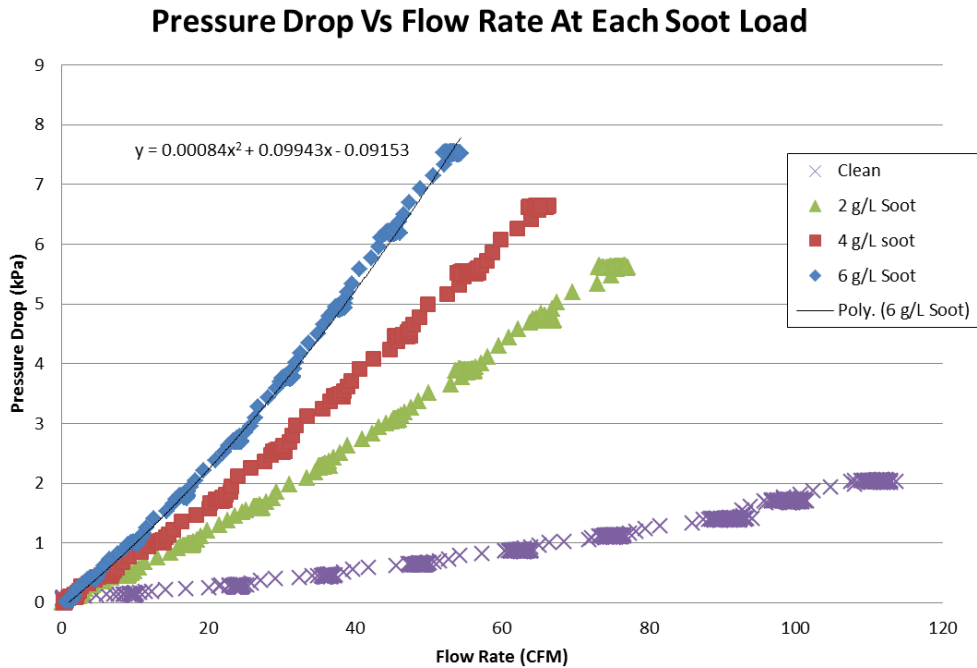
Pressure Drop Vs Flow Rate At Each Soot Load

$$y = 0.00084x^2 + 0.09943x - 0.09153$$

Legend:
- Clean
- 2 g/L Soot
- 4 g/L soot
- 6 g/L Soot
- Poly. (6 g/L Soot)

Axes: Pressure Drop (kPa) vs Flow Rate (CFM)

Figure 4.9: Sample Pressure Drop Data At Each Soot Loading Level

This is more evident in Figure 4.10 with all of the filter pressure drops plotted as a function of Soot loading at a constant 40,000 hr^{-1}. With no soot load, the clean pressure drop measurements of all of the filters are within 5% indicating that none of the filters are damaged. Even at this low soot loading resolution, the regimes of loading are clear in the pressure drop trend. Between 0 and 2 g/L, there is a steeper pressure drop slope during the deep bed filtration regime. After 2 g/L, the slope of the pressure drop curves are consistent between filters as a result of a uniform cake layer building up. The variation between filters primarily occurs in the deep bed regime. The standard deviation of the filters at 2 g/L is 0.21 kPa or 6.7% of the average pressure drop. A combination of variation in pore size distribution, filter manufacturing tolerances between filters, and smaller effects from error in mass and pressure measurement are likely the cause of this difference.
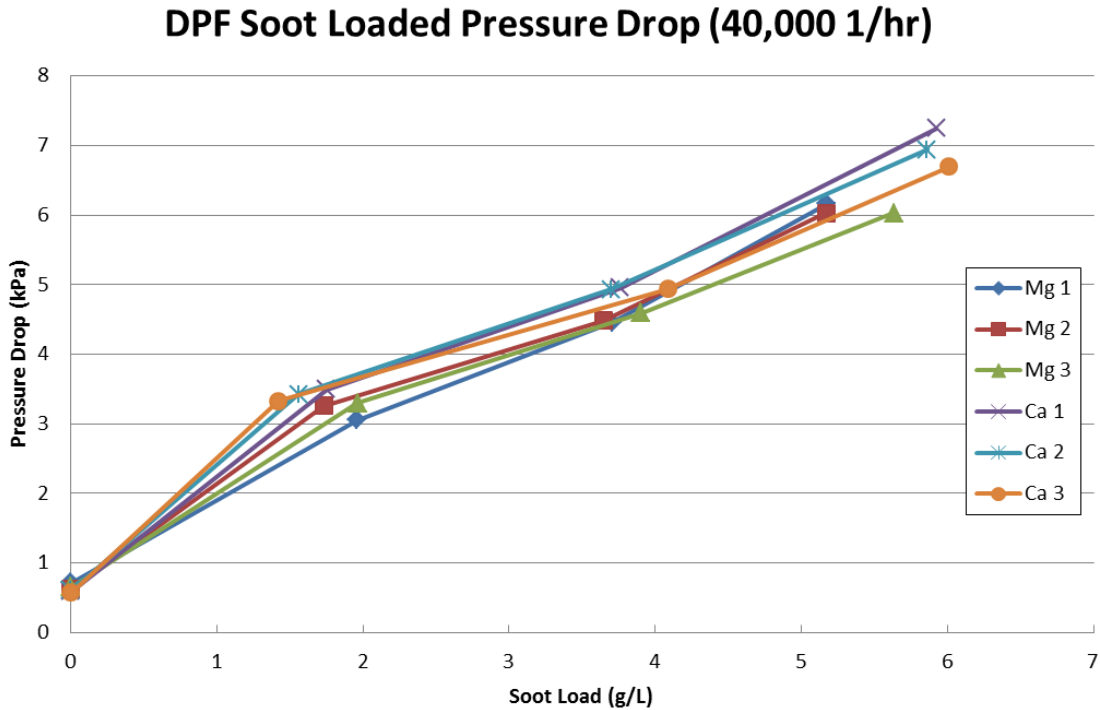
Figure 4.10: DPF Pressure Drop Increase Due to PM Loading for Normalization

Figure 4.11 shows the results for the three filters loaded with the high magnesium ash. At 3 g/L of ash loading, the average pressure drop increase is 0.5 kPa. All three filters seem to show a slow increase in pressure drop up to about 1.5 g/L followed by a slight increase in slope. This is a trend that is not captured in previous lower resolution data. Up to 3 g/L, the pressure drop data does not appear to leave the deep bed filtration regime which is supported by the imaging data in the next section. This is not apparent in previous data sets that seem to show the transition point occurring as low as 2 g/L. The large error bars on mass measurement and few number of points could account for this discrepancy.

There is high repeatability for this data set demonstrating the effectiveness of the accelerated ash loading system for repeatably depositing ash in the DPFs. The pressure drop has a maximum variability of 0.2 kPa in this measured deep bed filtration regime. This is similar to the variability seen in the soot loading tests meaning that filter variation and noise may account for a greater portion of the variation than ash deposition differences between filters.

Mg Ash Loaded DPF Pressure Drop (40,000 1/hr)
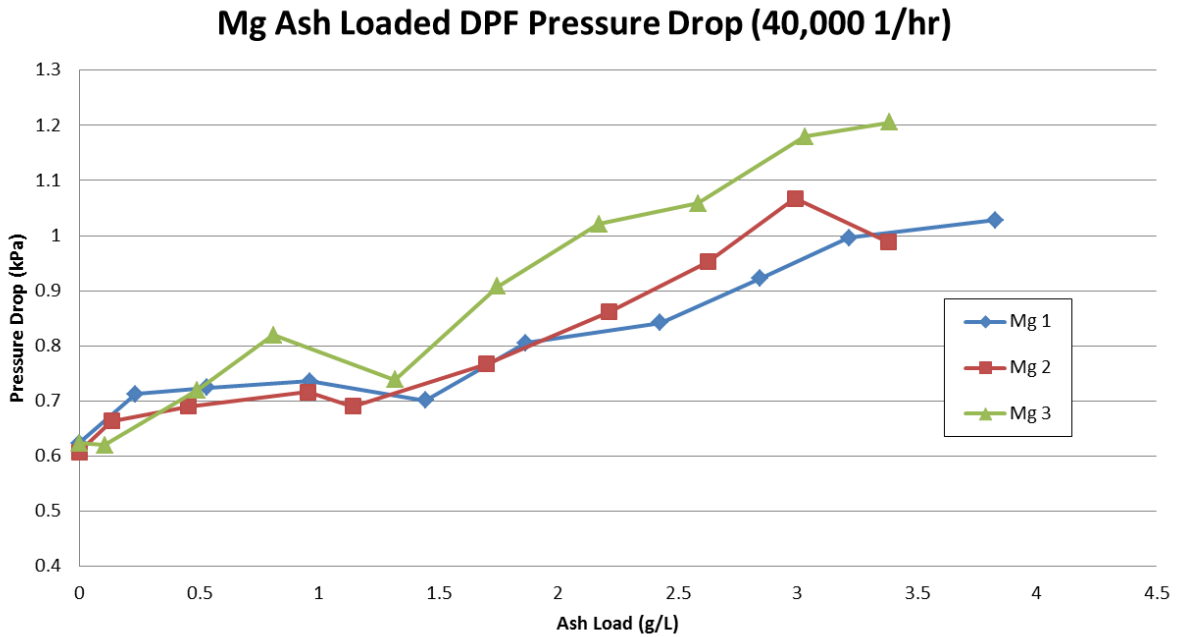
Figure 4.11: Pressure Drop vs Ash Load for Three Mg Ash Loaded Filters

Ca Ash Loaded DPF Pressure Drop (40,000 1/hr)

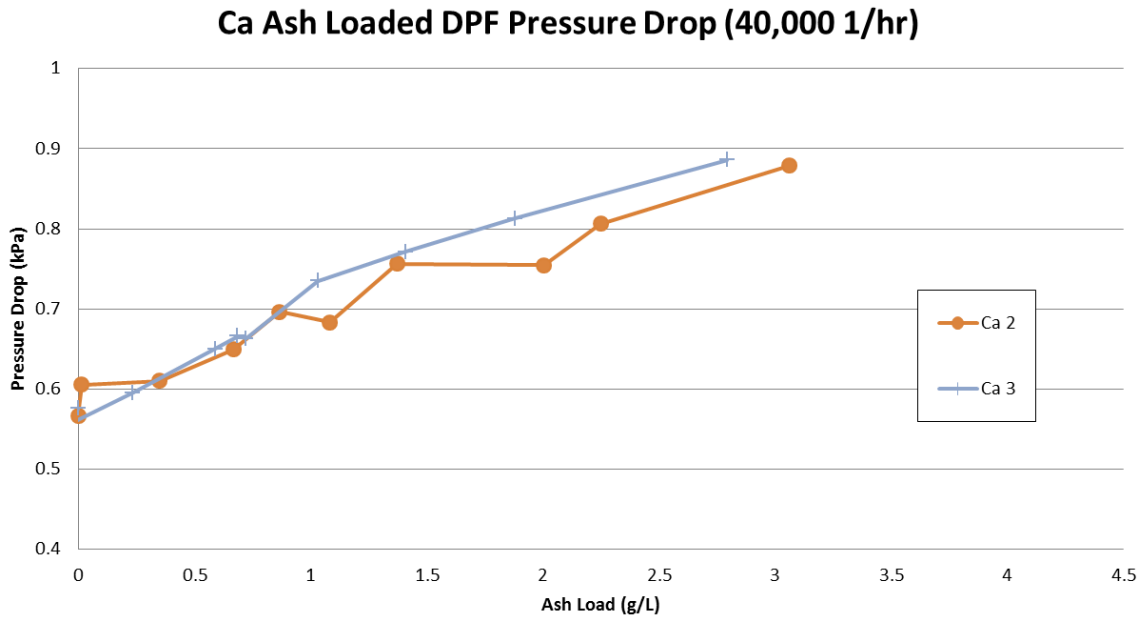**Figure 4.12:** Pressure Drop vs Ash Load for Remaining Two Ca Ash Loaded Filters

The pressure drop data for the high calcium ash loading tests are displayed in Figure 4.12. The first filter for this section of tests is not shown due to considerable cracking occurring during early loading stages. The cracking compromised the pressure drop measurements as a result of

large flow pathways being open that do not go through the porous walls. Figure 4.13 shows the cracking at the exit channels near the outside edge of the filter. The remaining two filters, however, show a very linear increase in pressure drop in the deep bed filtration regime. Again, there is no apparent transition point within the first 3 g/L. The variability is also lower than in the case of the high magnesium ash loaded filters.

Figure 4.13: Cracked Exit Channels on Ca Filter 1

In Figure 4.14, the pressure drop curves for both sets ash chemistries are overlaid. Unlike the results from the ash cake layer experiment, there does not appear to be a significant difference in trends between the two lubricant additive formulations. Since neither trend has reached the transition point up to 3 g/L, it is possible that additional loading up to and past the transition point may lead to differences in pressure drop if the transition point occurs in different places for each ash type. The pressure drop in the deep bed filtration regime is also the result of a complex interaction between a number of factors. The different ash morphologies may be interacting with the substrate in different ways that have competing effects and still result in similar pressure drops. This will be explored further in the following post mortem analysis. Additional efforts including more soot loading are also suggested to investigate additional differences in chemistry related ash deposition as a result of higher soot loading regenerations.
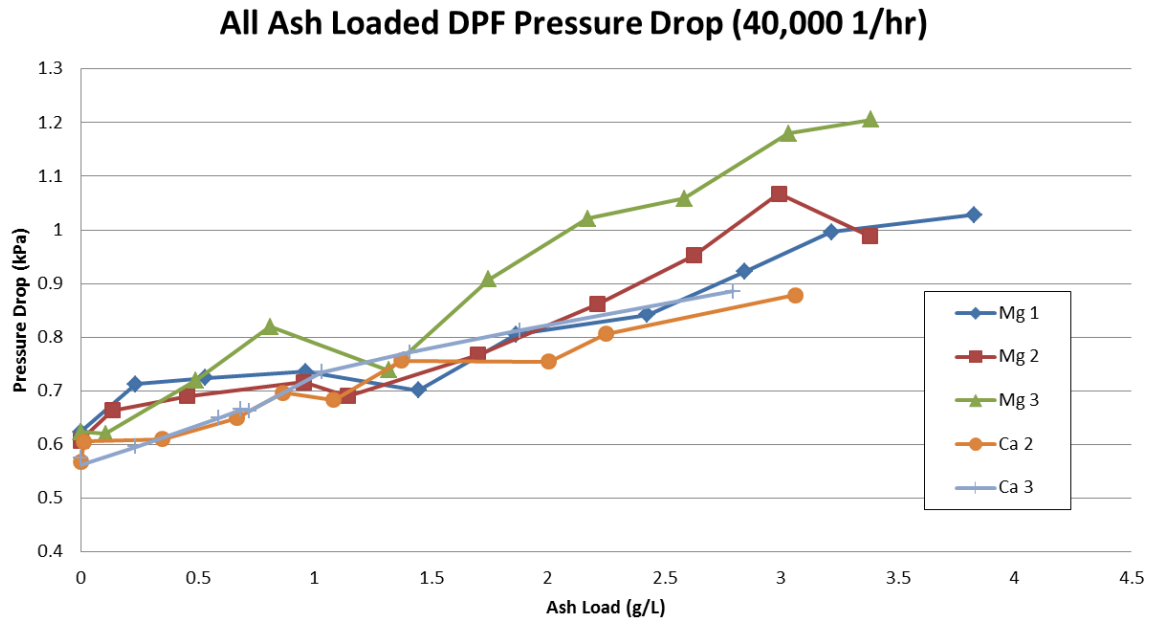
Figure 4.14: All Pressure Drop Vs Ash Load Measurements for Both Oil Types

This data can also be compared to previous low resolution pressure drop data using similar high calcium and high magnesium oils. As can be seen in Figure 4.15, the increase in pressure drop from this set of experiments was about half of that of the previous magnesium results and about one fifth of the previous calcium results. The difference in formulation is likely an important component of that difference in pressure drop. Also, the high tolerance in ash loading of about 2 g/L in either direction from the previous data means that the curve could be shifted significantly. Those experiments, however, did show a large difference in magnesium and calcium pressure drop. This, along with the following post mortem analysis motivates additional loading to see the continuing difference.
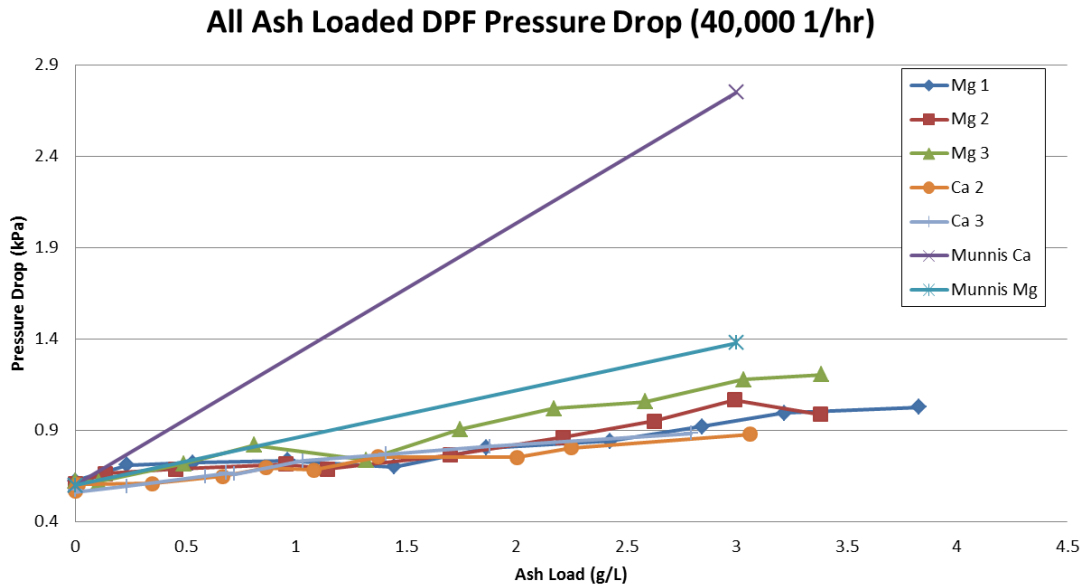
All Ash Loaded DPF Pressure Drop (40,000 1/hr)

Figure 4.15: Pressure Drop Data Overlaid with Previous Results

4.2.2. Post Mortem Analysis

In order to better understand the deposition mechanisms at this early loading stage, a post mortem analysis is conducted through the use of ESEM and X-Ray CT imaging. One of each of the partially loaded filters is sectioned so that small samples may be removed. Larger scale X-Ray CT imaging can be used to look at the general location of ash within the filters. At higher loading, the ash cake layer, mid channel deposits, and a large ash plug can be visible. However, at this 3 g/L loading, there is very little ash visible at this magnification and only a small amount of ash is forming the beginning of a plug section as seen in Figure 4.16.
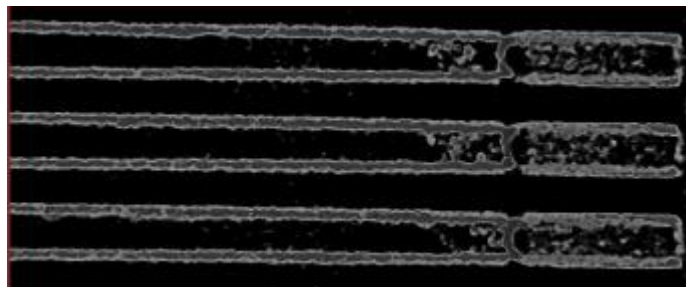

Figure 4.16: Low Resolution X-Ray CT Image of Ash Plug for Ca Ash Loaded Filter

65

Up to 3 g/L in both filters, there is no apparent cake layer buildup although some small amount of particles is in the plug section. At higher resolution, more details start to come into view. Figure 4.17 shows the inside surfaces of an inlet channel wall. The bright dots represent the magnesium ash particles that are spread evenly around the channel walls. These are large spherical particles that will initially fill the pores before turning into a cake layer. What is visible is the very beginnings of what will eventually become the ash cake layer after more ash deposition.
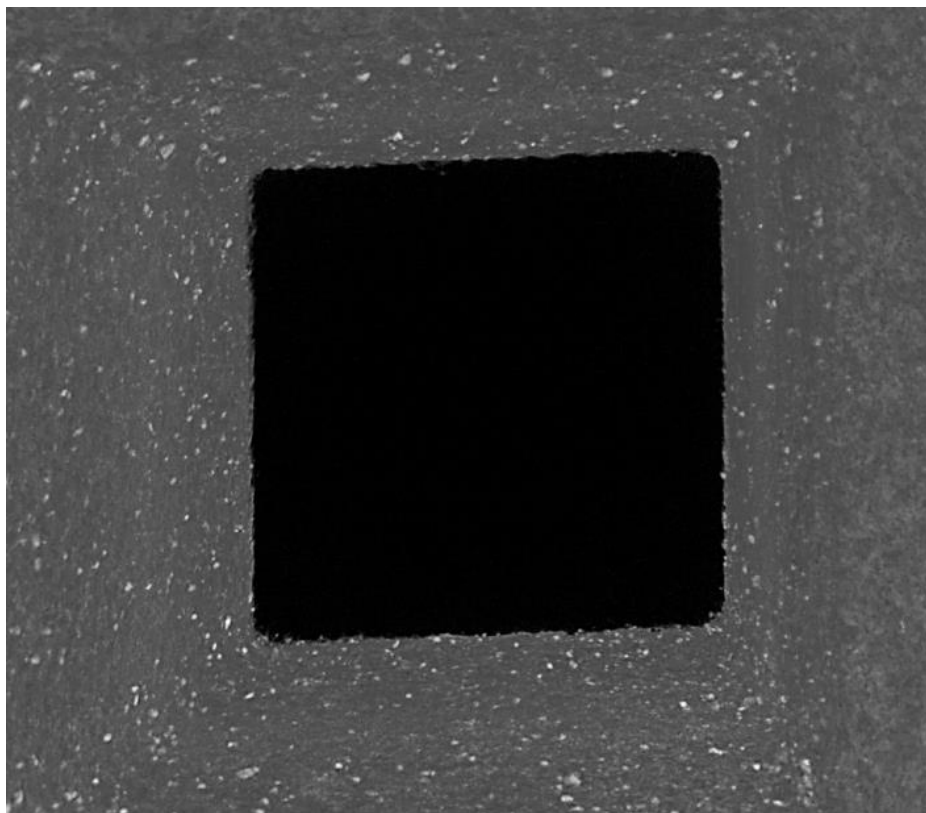
Figure 4.17: X-Ray CT Image of Inside of Mg Ash Loaded Inlet Channel

Significantly higher resolution ESEM images are able to provide clearer details into the differences in deposition between the two ash types. Figure 4.18 shows two representative instances of magnesium ash particles within surface pores in the inlet channel of the filter. Once again, the spherical morphology of the magnesium ash particles is clearly visible. In this case, there is significant penetration of particles into the pore to the point that much of the pores are filled. However, the ash particles within the pores appear to be loosely bound and porous.
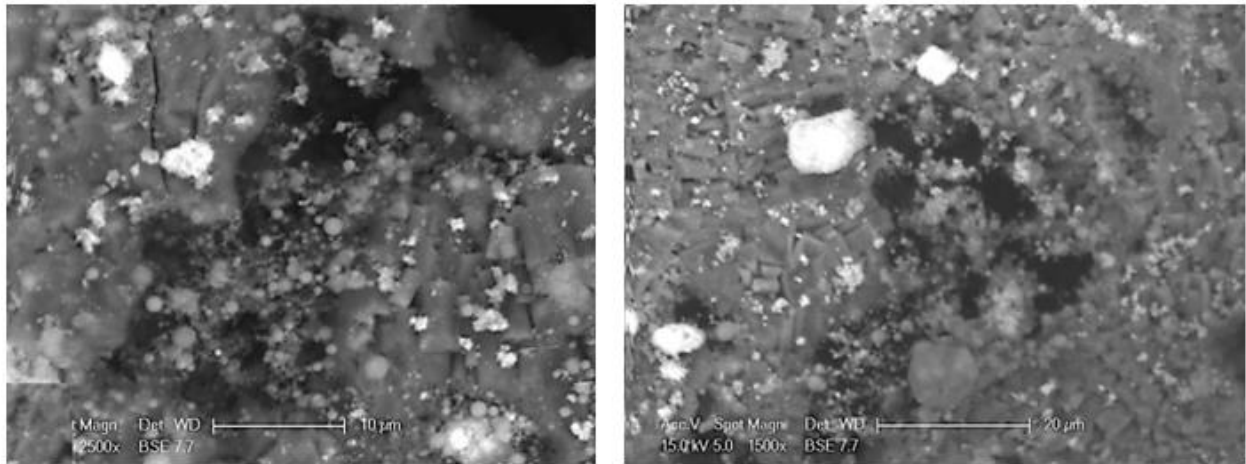
Figure 4.18: SEM Images of Mg Ash Loaded Surface Pores

There is a stark contrast between the deposition of the magnesium ash particles with that of the calcium ash. There does not appear to be a large amount of pore filling by calcium ash particles. The calcium particles are tightly clustered around the edges of the pores and have a dendritic structure. These structures also appear to stretch out into the opening and may be the early formation of pore bridging that can end up covering the top of a pore at higher loading.

Figure 4.19: SEM Images of Ca Ash Loaded Surface Pores

While the two pressure drop values are similar at 3 g/L of loading, the location and morphology of the ash deposits are quite different. The large amount of pore filling from the magnesium ash

may account for the slightly higher pressure drop at this ash loading. However, with only a small amount of pore volume left to fill, the magnesium ash loaded filters appear to reach the transition point ear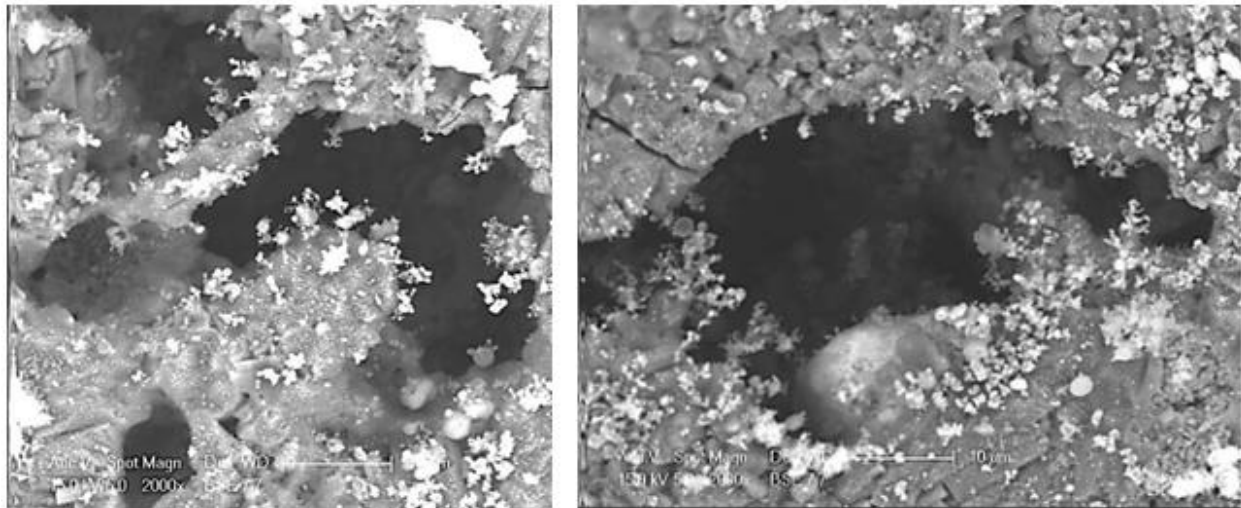lier than the calcium ash loaded filters. From previous experiments, we have seen the increase in pressure drop after the transition point slow substantially after the transition point has been reached. The calcium ash loaded filter, while only showing a slightly lower pressure drop, still has a substantial amount of unfilled pore volume. Unless complete pore bridging occurs before the pores are filled with ash, then the calcium is still well before the transition point and will continue on its initial slope.

Previous experiments such as those in [4] have shown just under a 2x increase in pressure drop due to deep bed filtration from single additive calcium ash than single additive magnesium ash. While this higher resolution experiment has not demonstrated such effects up to 3 g/L of loading, the details of the deep bed filtration described above may account for this difference. The use of high resolution imaging at this low ash loading has also provided a glimpse of a large difference in the deposition mechanisms between calcium and magnesium ash. Magnesium ash tends to quickly fill the pores with a porous cluster of ash particles while Calcium ash fills more slowly, clusters around the pore opening, and forms dendritic structures that extend out over the pore opening. The end result of both of these formations is a very similar pressure drop but these mechanisms can potentially be used to tailor the ash deposition to reduce future pressure drop at higher loading. And ideal loading case is one in which the pores are filled quickly but with as little flow restriction as possible so that the filter primarily resides in the cake layer regime. The high magnesium ash appears to have some characteristics of this trend. Additional experimentation to higher loading with similar post mortem analysis at higher loading is recommended to further investigate these mechanisms. A focus on soot level effects on regeneration and deposition is also recommended for a more complete picture.

(Page intentionally left blank)

5. ADVANCED DIAGNOSTIC ANALYSIS

As evidenced by Section 4.2, traditional analysis of DPF performance due to PM and ash loading include a combination of full filter flow and pressure drop measurements and micro scale post mortem analysis and imaging to understand exactly how particles are deposited, how they react to flow, temperature, and regeneration, and how they might be impacting the large scale pressure drop. While many important conclusions can be gleaned from such information, there is a disconnect between the microscale and macroscale data that requires further investigation. It is difficult to quantify how such micro scale effects as particle morphology, pore bridging, or ash sintering drive up the larger filter pressure drop.

The goal of this new area of advanced diagnostic analysis is to develop methods to create and use 3D image data from X-Ray Computed Tomography (X-Ray CT) scanning at a high enough resolution to capture microscale geometry. This allows for accurate 3D quantification of pore and particle characteristics and allows for the simulation of these microscale effects on flow. If local permeability variations can be measured due to local deposition effects or variations in filter geometry, this significantly improves modelling capabilities and helps to determine which operating conditions or lubricant additive formulations can help create the deposition that least increases pressure drop.

5.1. X-Ray CT Analysis

The primary tool used in this advanced diagnostic analysis is the X-Ray CT. X-Ray CT is a non-destructive imaging technique that generates 3D image data. This is done by placing a sample on a rotating stage between a source of X-Ray radiation and a detector. The detector captures a 2D projection of varying intensity of the sample based on the size, thickness, density, and material of the sample and how much of the X-Ray radiation is able to penetrate the sample and reach the detector. A number of these 2D projections are taken across a 360° rotation of the test sample providing a complete range of views of the sample. These 2D projections can then be computationally reconstructed into a 3D grayscale image based on the resultant intensity of each voxel that comprises the 3D image. [18]
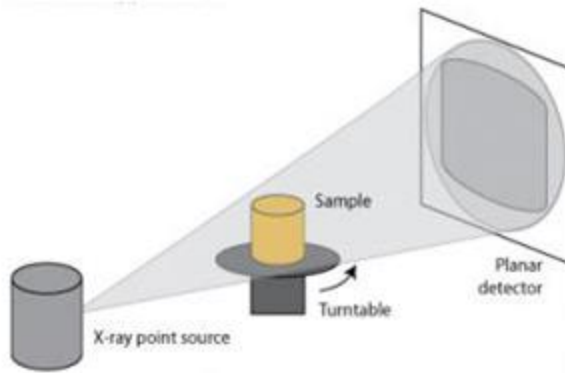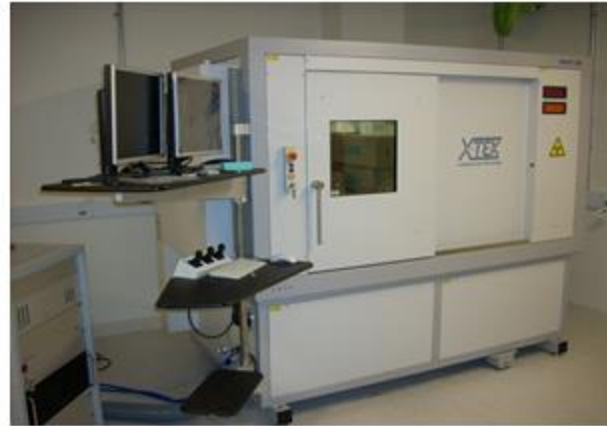
Figure 5.1: Diagram of X-Ray CT Source, Sample, and Detector Setup

Figure 5.1 shows the setup described above as well as its protective enclosure. The variable that controls the magnification of the sample is the distance between the sample and the source relative to the distance between the sample and the detector. The closer the sample is to the X-Ray source, the smaller the section of the sample that fits in the field of view and the larger it is magnified on the detector. For that reason, reaching the highest possible magnifications require using smaller sample sizes.

5.1.1. Background

Within the MIT group, the X-Ray CT has been used extensively to characterize ash location within the DPFs as well as relative ash density. This is done through a process that is demonstrated in Figure 5.2. First, a full size filter is scanned which gives good visibility of ash plug length and variation across the filter diameter as seen in (a). This is typically only beneficial at high ash loading or the ash layer may not be visible at this magnification. This level of scan is also useful for viewing any axial trends in the ash such as uniform gaps from mid channel deposits or possibly extreme temperature events in the filter. Next, the filter is broken into half or quarter sections to get a slightly increased magnification and reveal additional detail. In (b), a section of about 20x20 channels is shown which has the first region where smaller ash details start to become present. Here, larger sintered agglomerates are visible as well as spaces between each agglomerates. Some sense of high density regions compared to the rest can also be seen in the sections colored green.

At this resolution, the channel walls can be used as a rough density standard by which the ash density is compared. Ash that is a higher density than the wall is typically extremely tightly packed or sintered while ash that is lower or equal density to the wall is more of a standard packing density ash. Since different materials absorb X-Rays differently, the best density standard would be one using ash packed to a known packing density. After the 20x20 channel section, a sample as small as a 3x3 channel section is scanned which gives lots of information about density variation of the ash, ash cake layer thickness, and even some visibility of the pores within the walls. Even this resolution or the 2 channels in (d) are not a high enough resolution to recreate the pore network for either flow computation or quantitative values of pore or ash particle characteristics.
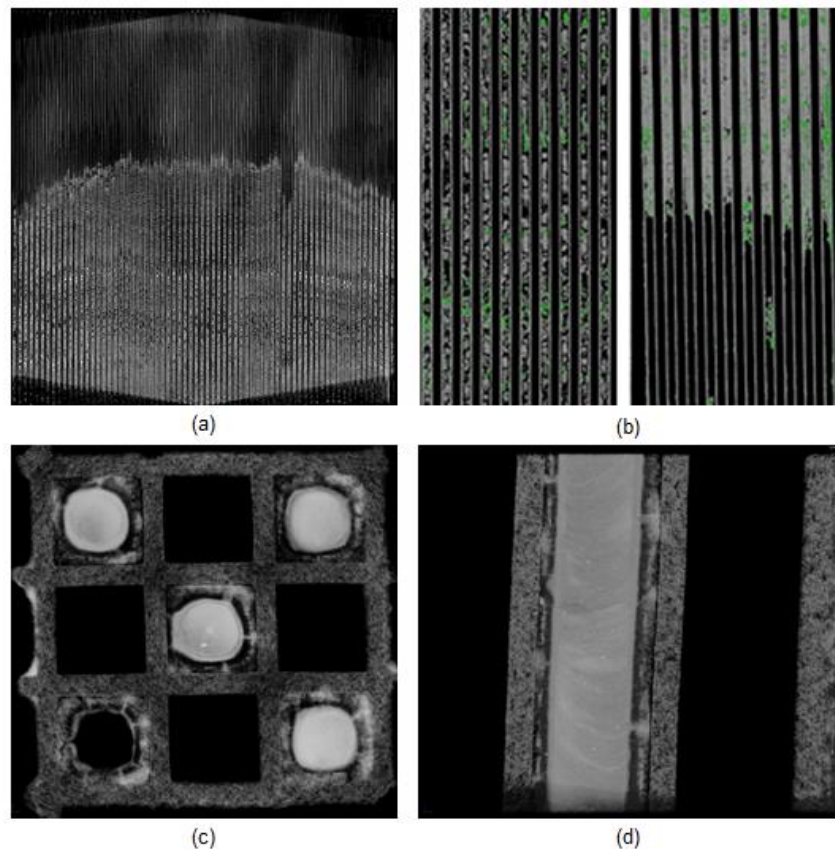

Figure 5.2: Typical Stepwise Process of Filter X-Ray CT Scanning Through Smaller Samples (Kamp)

This section explores new sample preparation, mounting methods, and tools to allow for the highest magnification scans possible beyond our previous capabilities. It will also explore comparisons with alternative imaging techniques such as SEM and the new details that can be captured. Additional post processing techniques will be shown to demonstrate how to convert from 3D greyscale image data to a segmented image that represents a 3D part that can be used in computational flow solvers.

5.1.2. Sample Preparation and Setup

As mentioned above, the method for increasing the magnification of the scan is to use a smaller sample and place it closer to the X-Ray source. In order to get the highest magnification possible, a single channel is scanned to reduce the required field of view. A single channel sample is chosen also because an enclosed inlet channel will not disturb the ash layer within while attempting to remove individual walls can displace the ash layer and provide an unrealistic picture of the ash deposition. During a typical scan at lower magnifications, a sample is fixed to a sample holder in some fashion. The sample holder is then placed into a slot in the stage and is tightened with a set screw. The stage is then rotated during the scan allowing for images to be taken at all angles of rotation. The center of rotation of the stage is typically close enough to the center of the part relative to the size of the part that any difference is negligible.

At the highest magnifications with a field of view on the order of 1 mm, the difference in part center and stage center of rotation becomes extremely critical as shown in Figure 5.3. In that example, the majority of the sample will not actually be in the field of view during the full rotation about the stage center and the image will not reconstruct due to missing data. The full sample needs to stay within the field of view during the whole scan. At this scale, the mounting method and stack up of connection tolerances can easily separate the two centers of rotation if they are not tightly controlled.
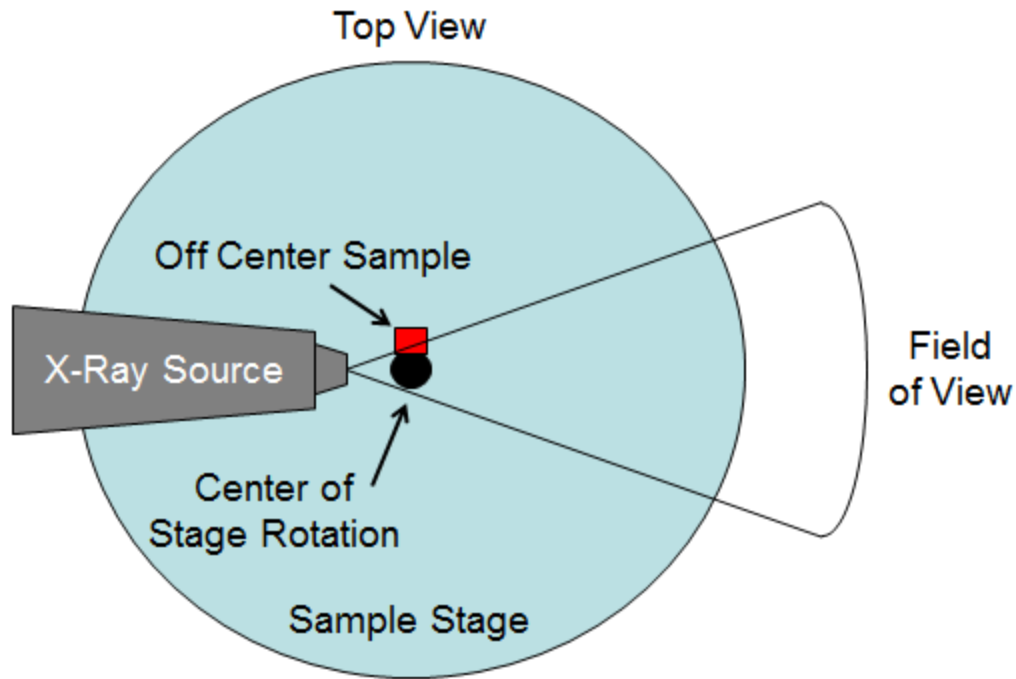
Figure 5.3: Diagram of Loss of View of Non-Centered Sample at High Magnification

This requires a holder that can accurately center one vertically oriented channel about the stage center. Rather than use a clamp type holder or simply attaching a sample to the stage surface with foam and tape as has been done in the past, an aluminum channel holder is fixed to an existing platform through a slip fit in its center hole and tightened with a set screw. The top of the aluminum channel holder is machined down to fit tightly inside the single channel with a seat to hold its position. The described holder is shown below in Figure 5.4.

This holder is designed to center the holder as much as possible about the stage by using the inherent centering properties of the mounting holes on the system. The only remaining source of offset is the tolerance stack up between each of the clearance fits in the mounting holes. Even at this magnification, this is relatively small compared to the field of view. The reconstruction software is also robust to small offsets during the reconstruction procedure.
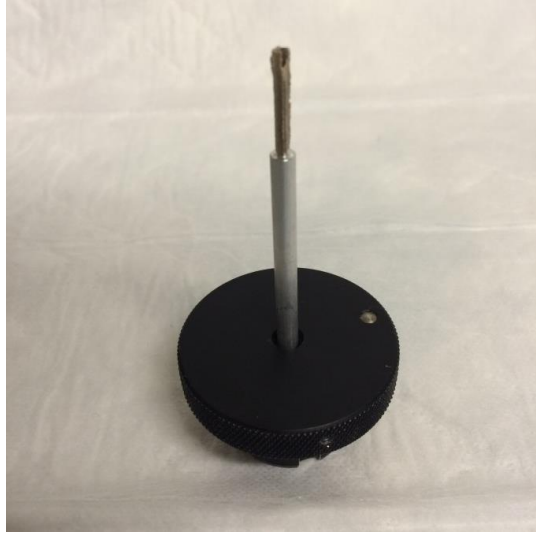
Figure 5.4: Single Channel Holder to Center the Filter Sample

This setup was used with a number of single channel samples as described in section 5.1.3. It is important to note that there are two available types of X-Ray sources for this setup. The first, and typical setup is the reflection source which sends high energy electrons into a small tungsten mass that acts as the X-Ray source and sends out X-Rays in all directions. A small window about 6 mm away acts to narrow the useful X-Rays to the field of view used in the scan before they finally hit the detector. This setup can run at fairly a fairly high power of up to 6 W.

The second available source to use is called the transmission source. This is the end portion of the system that can be swapped out. Similar to the reflection source, it uses high energy electrons that hit tungsten. The difference is that the system is oriented in a straight line rather than a 135° reflection at the tungsten mass. The electrons are sent directly towards the exit window which is coated in a tungsten film. The beam must penetrate the film and energize the tungsten through the thickness for it to produce X-Rays out towards the sample. This system can only handle 3 W of power and produces a slightly lower intensity image due to the lower power and the weaker production of X-Rays through the thickness. The benefit of this system is there is no gap between the source and the window so the sample can be placed closer to the source and in a smaller field of view. This results in a higher magnification.

In order to also scan these samples at a higher magnification under the transmission source, additional mounting improvements need to be made. The tolerance stack up mentioned previously is no longer acceptable under the new available magnification and the sample needs to be perfectly centered. Rather than modify the mounting structures that are available with the system, it is easier to control the relative position of the part center with the stage center. This is done through the use of a precision X-Y slider stage mounted between the stage and the sample holder. This slider stage is shown in Figure 5.5.
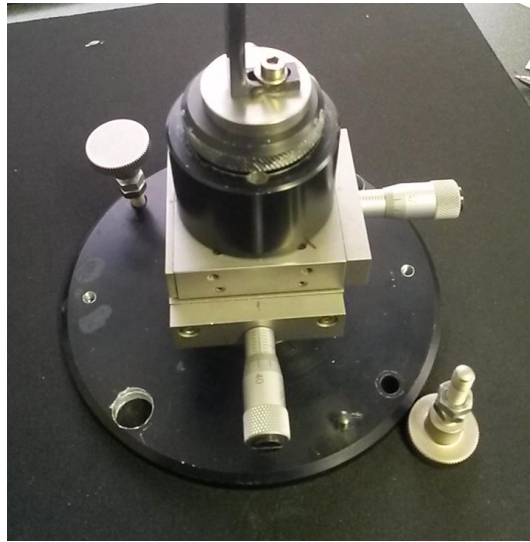

Figure 5.5: X-Y Slider Stage for Precise Sample Centering

Once the slider is fixed to the rotating stage and the sample is fixed to the top of the slider, an iterative process is then used to center the part within the field of view. The part is rotated so one set of adjustment is perpendicular to the direction of X-Rays. It is adjusted until it is centered on the 2D image. The part is then rotated 90 degrees and adjusted the same way. Once the part has no wobble in the 2D image through the full range of rotation, the sample is ready to be scanned. As a result of the lower intensity of the transmission source images, noise becomes a more significant issue to overcome. To mitigate this issue, four times the number of background images are taken to reduce background noise. In addition, four projections are averaged at each angle of rotation rather than a single image to reduce the effect of background noise. These two effects combined reduce the noise to an acceptable level but also increase the scan time required.

5.1.3. Test Plan

In order to explore the capability and resolution of this system using the updated mounting and scanning methods, a range of samples needs to be scanned and processed. First, three samples will be taken from clean filters with no ash. Two of them are uncoated while the third has a wash coat. Next, three samples with different ash chemistries are selected from the work described in [4]. This includes a typical CJ-4 ash and single additive magnesium and calcium ash. Finally, one sample with CJ-4 ash generated in the field is selected. In addition, scans are made using both the reflection source and the transmission source to explore the benefits of each and viability. The full list of samples and scans are shown below in Table 5.1.

Table 5.1: List of Samples Scanned Using X-Ray CT and Type of Scan

Sample	Sample Type	Filter Type	Scan Type
1	Clean Uncoated	200 CPSI	R
2	Clean Uncoated	300 CPSI	R
3	Clean Coated	300 CPSI	R
4	Lab Loaded CJ4	300 CPSI	R/T
5	Lab Loaded Mg	300 CPSI	R/T
6	Lab Loaded Ca	300 CPSI	R/T
7	Field Loaded CJ4	300 CPSI	R/T
8	Lab Generated CJ4	Ash Sample	T

There are two distinct modes in size distribution of the geometry in a porous cordierite system with ash particles. The first is the pore sizes themselves which typically vary from around 5 µm to as high as 60+ µm. This size is determined by the manufacturer specification as well as how tightly the pore size distribution is controlled. An average size of 15 – 30 µm is common. The second mode of critical sizes is that of ash particle size distribution. This can vary from primary ash particles around 1 – 10 µm to large sintered agglomerates that can become as large as 100 µm.

Both types of X-Ray sources are capable of reaching magnifications high enough to fully capture the pore network structure. For this reason, the clean filter samples with and without the washcoat are done with the reflection source. Having an accurate representation of the pore network allows for accurate measure of porosity, pore sizes, and simulation of filter

permeability. The reflection source is also capable of capturing a wide range of ash particle sizes. However, at the smallest ash particle sizes, there is difficulty in fully capturing the ash geometry. The additional resolution from the transmission source provides a comparison with the reflection source to fully model the ash cake layer. For each type of ash loaded filter, scans were done with both the transmission source and reflection source. Finally, in order to achieve the highest possible resolution possible with this system, a small amount of loose CJ4 field ash is packed into a narrow glass tube measuring 500 μm in diameter. This is then brought as close to the viewing window as possible to capture the ash geometry. The combination of these different scanning methods and samples provide a solid baseline of knowledge and methodology for high resolution DPF scans in the future.

5.2.   Image Processing and Analysis

The following sections first look at the imaging results primarily using the reflection source and investigate the new filter and ash details available at this new resolution. Additional comparisons will be made with other more typical high resolution tools like ESEM and FIB. The methods to convert from grayscale image data to binary segmented data that can be used in simulation will also be viewed. Finally, results of simple simulation efforts will be shown to demonstrate the viability of this new capability as a tool for further study.

5.2.1. Imaging Results

Using the high resolution data available from the single channel scans of various samples, a range of new details become clear that were previously only accessible from SEM imaging. Below in Figure 5.6, a 2D slice through the walls of a single coated channel from Case 3 is shown in conjunction with a previous example of high resolution imaging using the X-Ray CT under previous methods. The white portion of the image corresponds to the cordierite material of the 4 walls of a channel in the DPF. The dark portion is void space in the image. The most notable difference between the two images is the visualization of the full pore network and complex pore structure of the channel walls in the right hand image. It is possible to qualitatively (and later quantitatively) see the variation in pore size, location of large pores through the wall thickness, and imperfect straight lines from manufacturing tolerances. For example, there are

clear instances of especially large pores on the top of the right hand wall as well as the bottom wall near the center that could create locally high porosity as well as weak portions of the wall that could later result in cracking. There are also sections like the portions of the bottom wall that have a particularly low porosity. These are all important characteristics that become clear at this higher magnification.
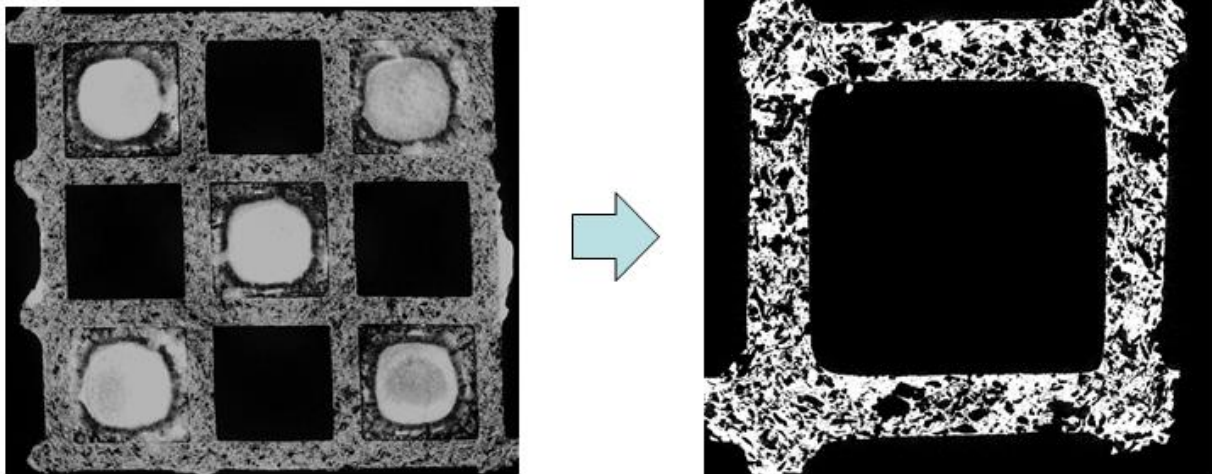

Figure 5.6: Comparison of Previous Highest Resolution CT Image with Early Results of Coated Single Channel Using New Methods

This is also just an example from one 2D slice of the available image data. As shown in Figure 5.7, the data can also be viewed as a 3D image showing the full complex porous geometry. The left sample is from Case 3 and the right sample is from Case 2. These represent a small axial slice of a single channel of the coated and uncoated filter samples. A number of scans can be taken from different sections of the filter to gain a more complete view of internal filter variation.
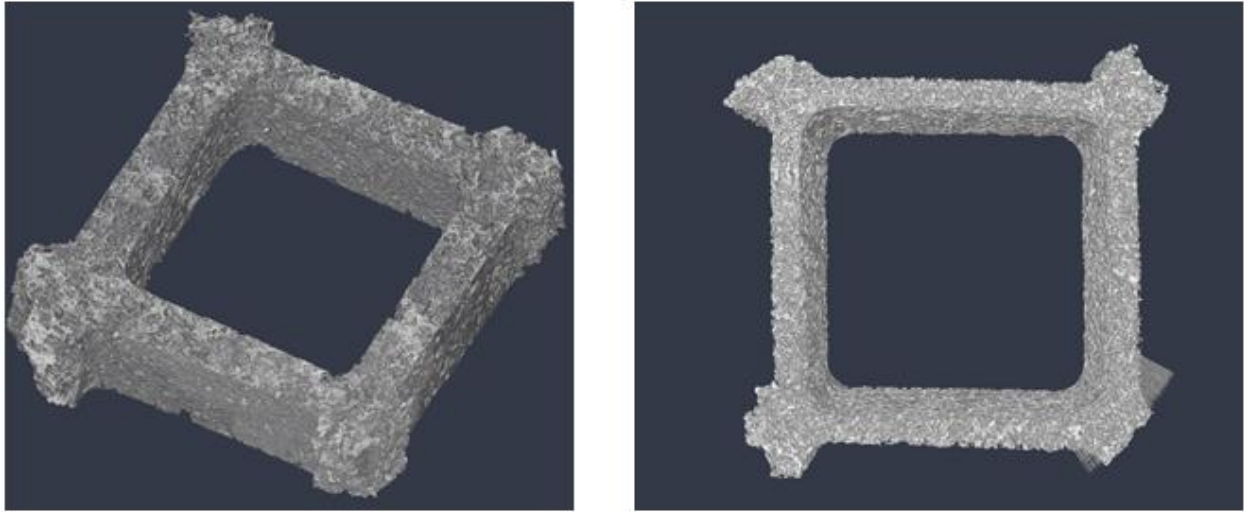
Figure 5.7: Samples of 3D data of Single Channels of Clean Coated (left, Case 3) and Clean Uncoated (right, Case 2) Filters

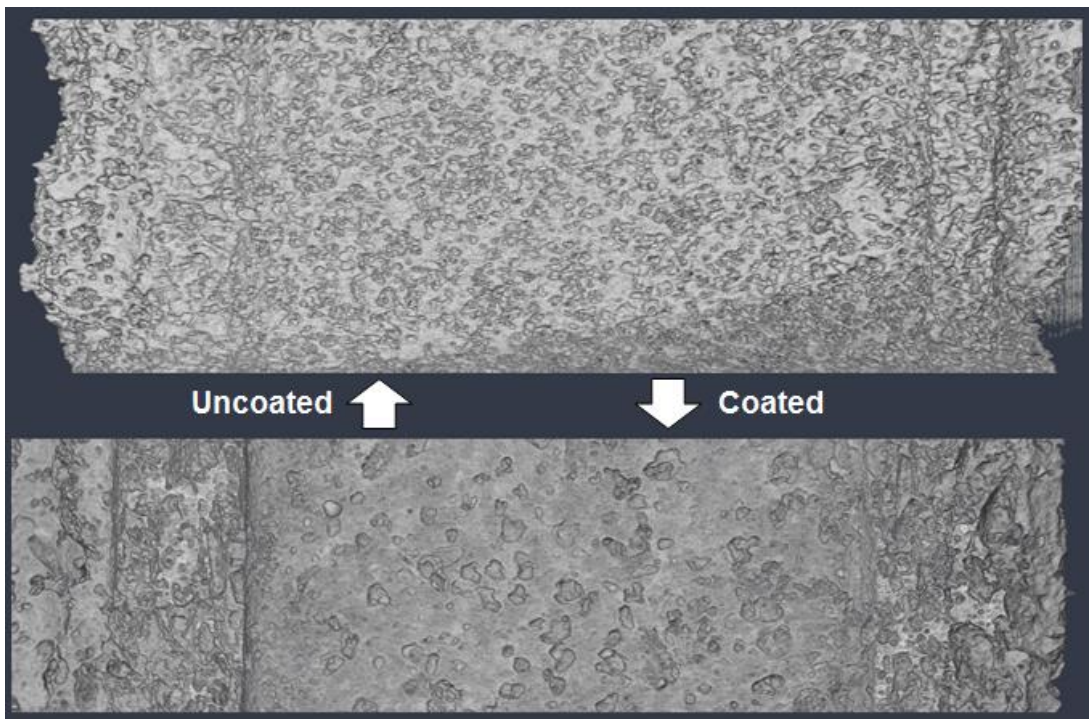**Figure 5.8:** Difference in Channel Wall Surface Between Clean Uncoated (Case 2) and Clean Coated Samples (Case 3)

Looking at these two samples from a side view perpendicular to the channel walls, there is a clear difference in the surface properties of the samples. This is due primarily to the existence of the washcoat on the coated sample. The washcoat deposits material on the top layer of the

cordierite and fills in a significant number of smaller pores on the surface. What is left is a number of much larger pores that have been shrunken slightly but are still apparent on the surface. The existence of the washcoat material has a large effect on both the physical appearance of the channel wall and its flow restriction. In Figure 5.9 and Figure 5.10 below, the surfaces of each of the filter types are compared with ESEM images to see the detail captured in the CT imaging. The wide variation in pore size opening is visible in both versions of the uncoated filter while the coated samples only have pore sizes on the order of 20 μm. The SEM images also only show the details of the top surface while even small depths into the pores soon no longer become visible as it becomes difficult for electrons to be able to return to the detector. The CT image shows every part of the pore geometry that is visible from the surface from this angle.
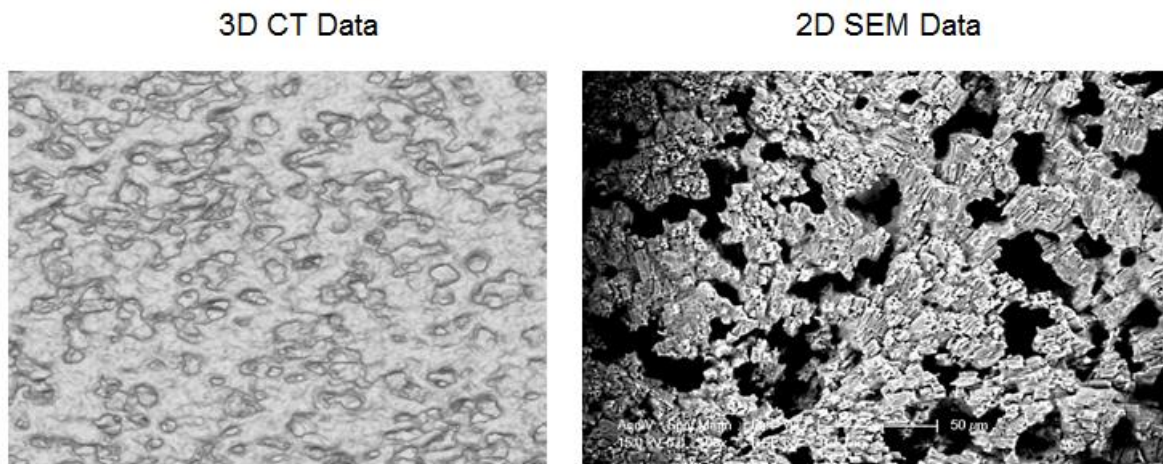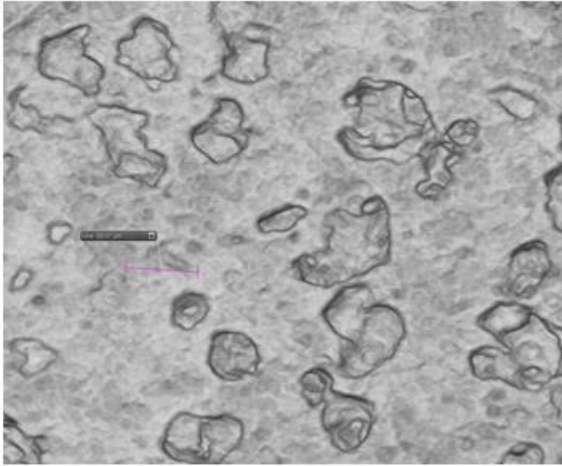

Figure 5.9: Side by Side Comparison of Clean Uncoated Filter Surface with SEM Image (Case 2)
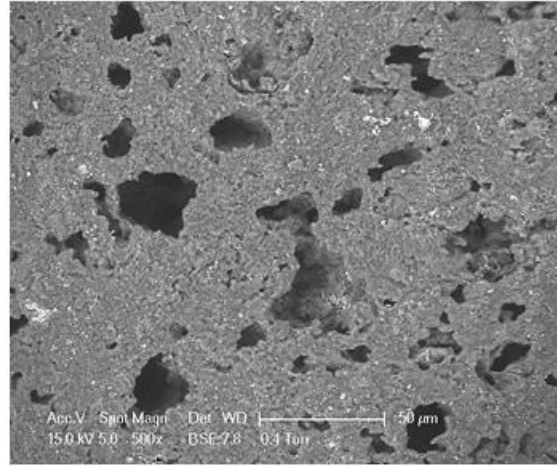
Figure 5.10: Side by Side Comparison of Clean Coated Filter Surface with SEM Image (Case 3)

Because these images include full 3D image data, it is possible to slice the image at any point to look at interesting geometry. The previous method for looking into the pores of a sample or to cut into the cross section of a wall or particle required FIB milling. Some examples of this are shown below in Figure 5.11 and Figure 5.12. The first shows an example of slicing through several large porous ash particles with an example of a similar particle that has been cut with FIB milling and imaged using SEM. This is a time consuming process that only allows for slicing at one location at a time after it has already been determined to be a valuable section. 3D CT scans allow for effectively infinite FIB slices to gather significantly more data. The left image in Figure 5.12 shows a 2D slice of the CT data demonstrating ash buildup in the surface pores. A comparison with a similar SEM example is also shown. This is an example of one limitation of the resolution of the reflection source imaging with the CT. While much of the ash detail is available, the SEM can still reach a slightly higher magnification and remains a beneficial tool. The CT, however, can still be used to show ash penetration in many pores within the filter with relative ease in comparison.
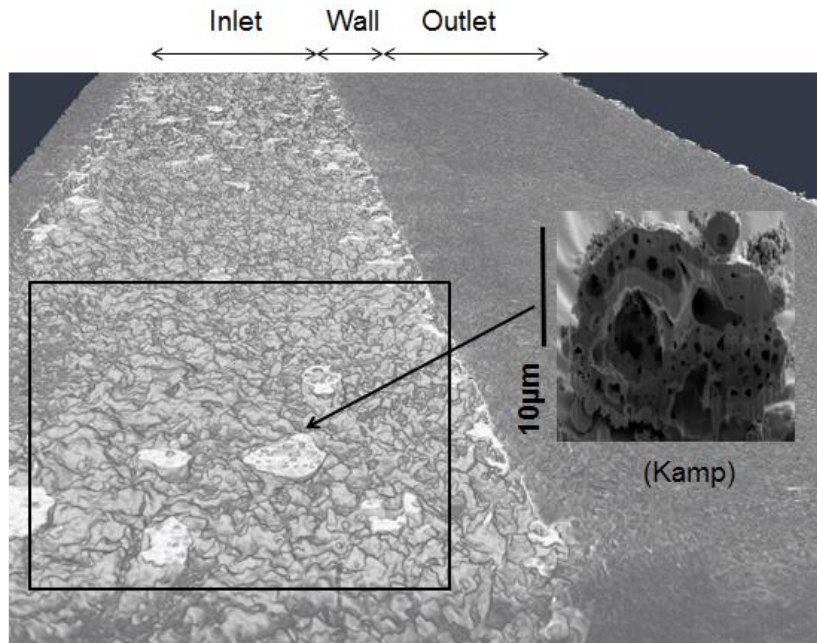
Figure 5.11: Slice Through Large Porous Ash Particle Compared to FIB and SEM Image
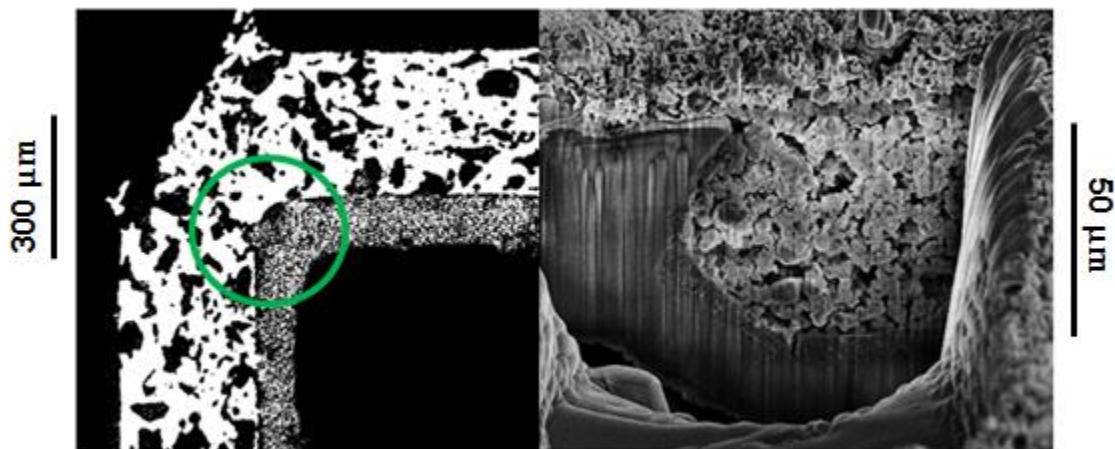
Figure 5.12: 2D CT Slice (left) Demonstrating Ash in Surface Pores Compared With SEM Image (right)(Kamp)

The field sample from Case 7 is shown below in Figure 5.13. In this image, a fiber particle is visible sticking out from the right hand wall. This particle is derived from upstream packing material in the exhaust system. There has been previous indication of fiber particles becoming entrained in the flow and being caught in the DPF. These types of particles have a diameter of 5 μm which is still captured in these scans.
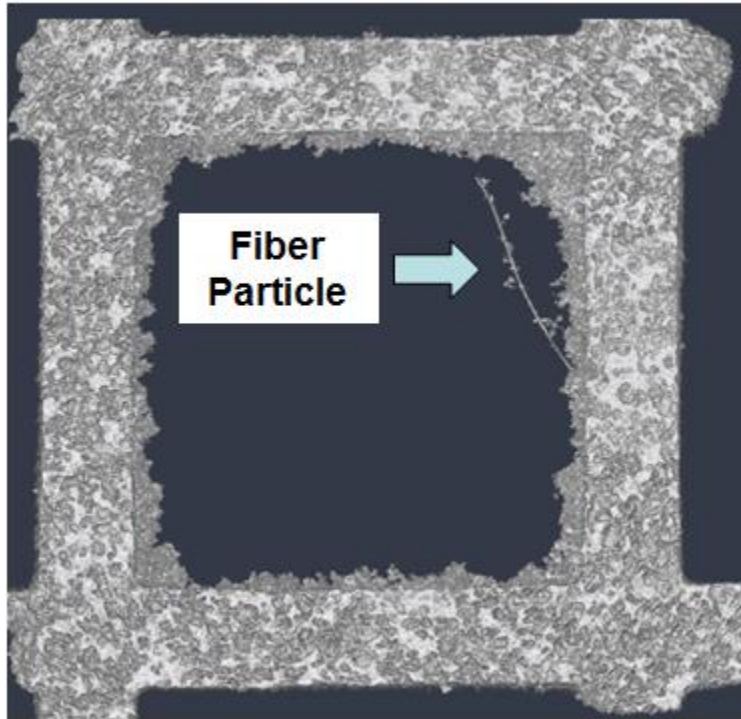
Figure 5.13: 3D Image of Field Generated Ash Loaded Sample From Case 7

Figure 5.14 shows a side by side comparison of the single additive ash loaded channels from Case 5 and 6 using magnesium and calcium. Looking first at image (a), the calcium ash cake layer is made from a tightly packed layer of very small spherical particles of about $2 - 5$ μm in diameter. The magnesium ash in image (b) also consists of spherical particles but the diameter can be as large as 50 μm. This follows what is expected from the TEM images of morphology. The larger particle size also explains the lower pressure drop due to the higher permeability from the Kozeny-Carman equation. In addition, the magnesium particles in image (b) appear to be much more loosely bound as demonstrated by the particles detached from the wall.

84

Figure 5.14: Side by Side Comparison of Single Additive Ash Types from Case 5 (b) and Case 6 (a)

5.2.2. Segmentation Methods

To convert the grayscale image data to binary data that determines what area is material or what is air or void space, the 3D data has to undergo segmentation. Segmentation is the process by which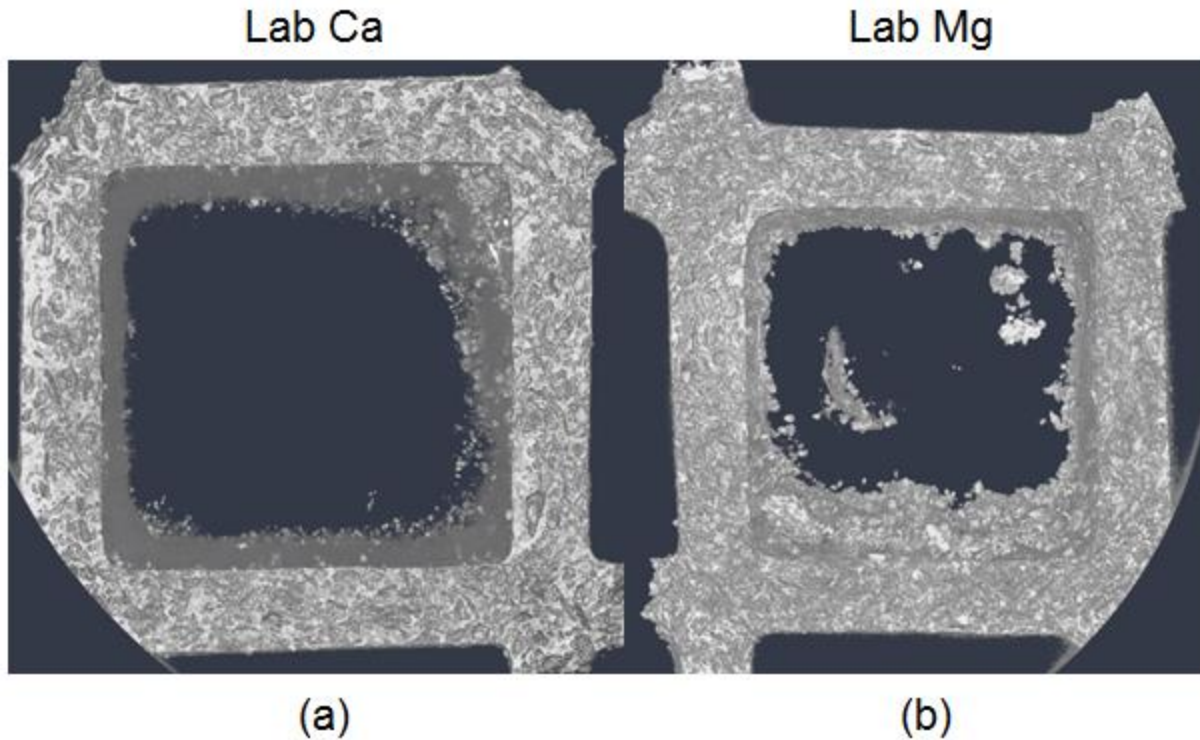 each voxel is determined to be a component or void (1 or 0). While image processing and segmentation is a significant field of its own, two main methods were selected for use on these samples due to simplicity and to avoid removing details from the images themselves.

The first and most basic method of segmentation is called a threshold segmentation. With every voxel in the image assigned a certain grayscale value, a histogram of grayscales can be generated to see the distribution. A threshold segmentation chooses a value by which everything on one side of the threshold is material and everything on the other side of the value is not. Separate peaks in a histogram typically represent different materials and can be reasonably separated but in many cases there is some overlap. Figure 5.15 shows the histogram of a clean filter. The two distinct peaks represent the volumes associated with cordierite in the filter and air in the pore

spaces. Depending on the threshold chosen, the measured porosity of the filter sample varies significantly. Without a clear cutoff point, it is necessary to have a porosity standard by which the threshold can be accurately chosen. This can consist of an external sample of known porosity that is included in the scan with the sample of interest. Due to the small sample size this is difficult to do. A simple option for these types of samples is to choose a threshold that provides a porosity that coincides with the manufacturer specification. While this is a reasonable method to use the filter itself as the density standard, the tolerances of the manufacturer specification cannot always be relied upon. This means that in many cases, the alternative method described below is more reliable for segmenting the sample.
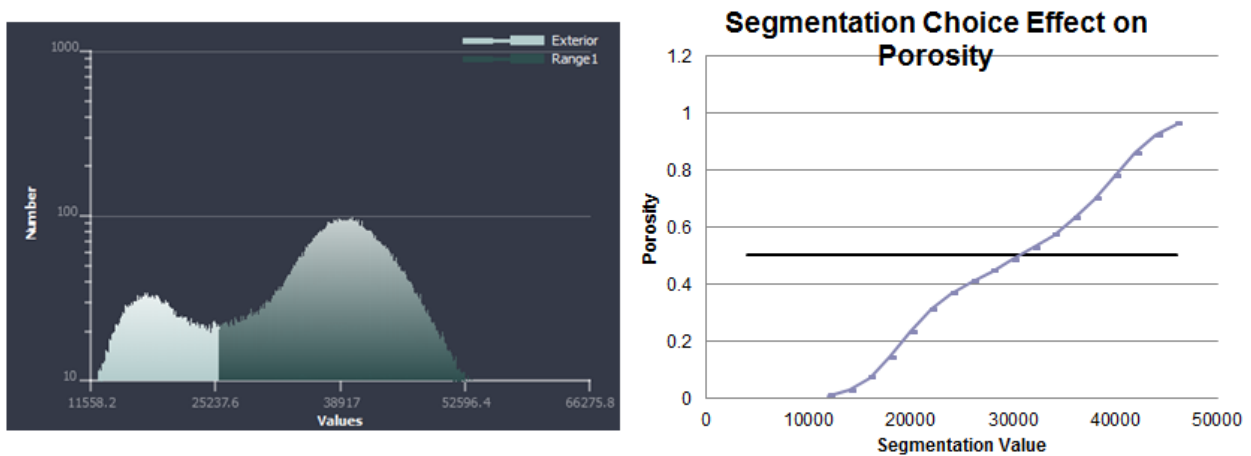
Figure 5.15: Image Grayscale Histogram and Threshold Effect on Measured Filter Porosity

The second method for segmentation includes a complex algorithm built into the image processing software that is used. This method is called a marker based segmentation. To do this, separate materials for the filter and void space are created. Then, regions of the histogram are chosen manually and put into one of the material categories. By using small sections of the histogram, regions of extremely high confidence of their material type can be chosen such as opposite sides of the histogram and far from the overlapping region. While only a small amount of the full image has been selected and put into material categories, this small section acts to seed the image for further calculation. Next, a gradient image is calculated on the full 3D image. This finds the regions of highest image gradient which corresponds with the surfaces between different materials or between the filter and air. The marker based segmentation algorithm then

86

starts with the seeded points and fills out the entire image, assigning materials to each voxel and using the gradient image as edges for the material regions. After testing this method on five clean filter sample sections, each resulted in a porosity measurement within 5% of the manufacturer specification which gives high confidence in the method and accounts for local variations within the filter.

5.2.3. Porosity Results

After the samples have been segmented, a binary 3D data set remains with 1 or 0 labeled voxels. An example of this type of data set with a small section of filter wall and ash cake layer from Case 6 is shown below in Figure 5.16.
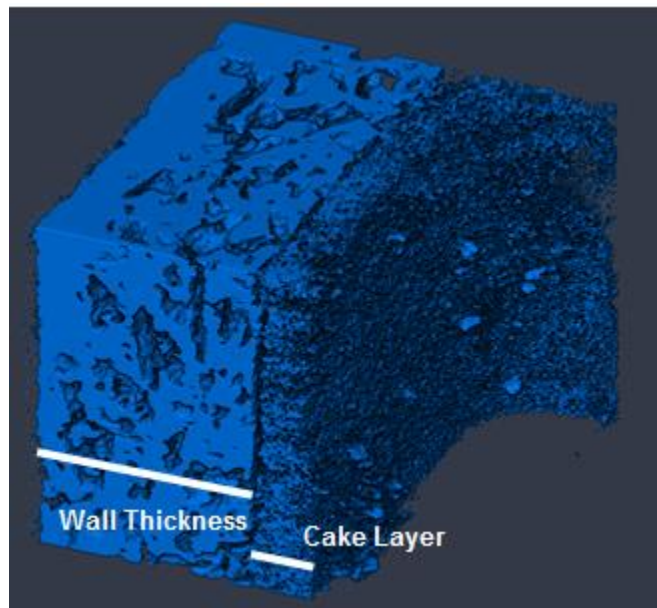
Figure 5.16: Segmented Subsection of Filter Wall and Ash Cake Layer

Using a binary data set, it is a simple task to count the number of void voxels and compare it with the total number of voxels to calculate porosity. In previous porosity analysis, porosity of the filter was calculated from 2D images either looking at the filter surface or from a 2D image of a wall cross section. While this method works for finding porosity, it is a narrow method since it does not take into consideration local variation in pores and may give an artificially high or low porosity value. In order to compare the 2D porosity analysis with the newly available

volume porosity, the porosity at 10 slices through the filter wall is compared with the volume porosity across that region. Figure 5.17 shows the 2D slices and 3D volume used to test this comparison. The results are shown in Figure 5.18 where the slices are chosen in the axial direction. The actual volume porosity can vary a few percent from the individual slice porosities due to local variation. The tolerance on pore size distribution is also responsible for this local variation since a high pore size distribution can lead to very high porosity regions with large pores or regions of very low porosity. The pore size distribution is also a key filter parameter that can be calculated using this data for purposes of comparing with manufacturer specifications and for investigating the effects on ash deposition and flow restriction.
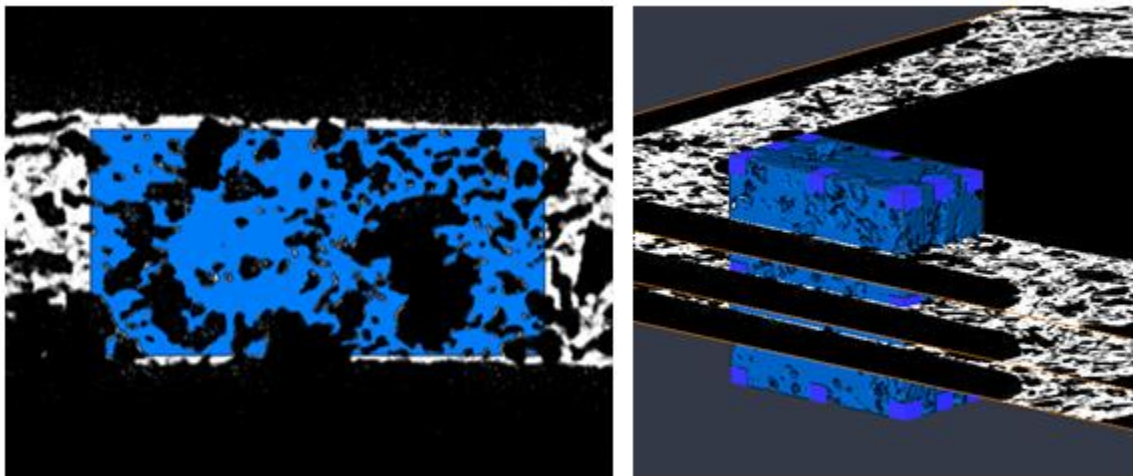
Figure 5.17: Region of Measured Porosity in 2D Slice (left) vs Region of Measured Volume Porosity Over All Slices (right)
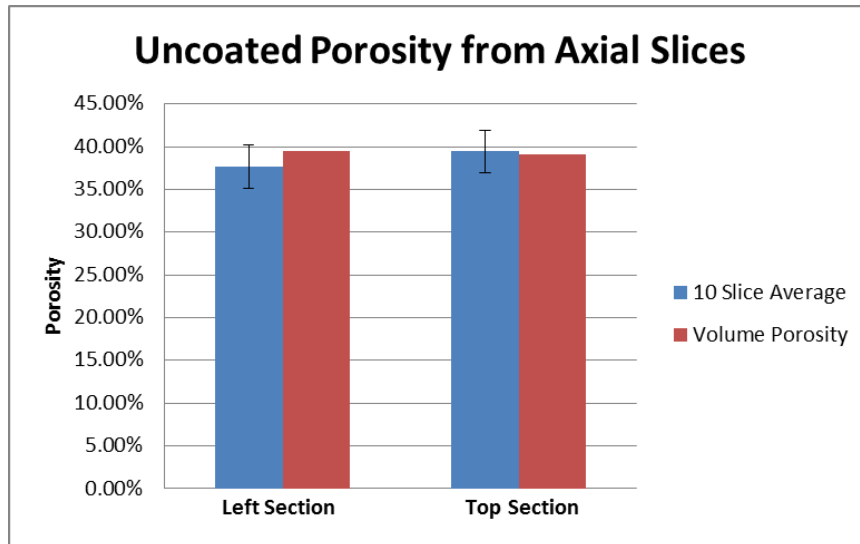
Figure 5.18: Comparison of Porosity of 10 Slice Average vs Volume Porosity of Two Filter Sections of Case 1

The data shown above demonstrates the effectiveness of using a volume porosity for porosity calculations within the filter. While there is a small amount of porosity variation along the length of the filter, the presence of the washcoat on the surfaces of the channel walls can have an effect on the porosity variation across the thickness of the filter. This porosity variation is demonstrated in Figure 5.19.
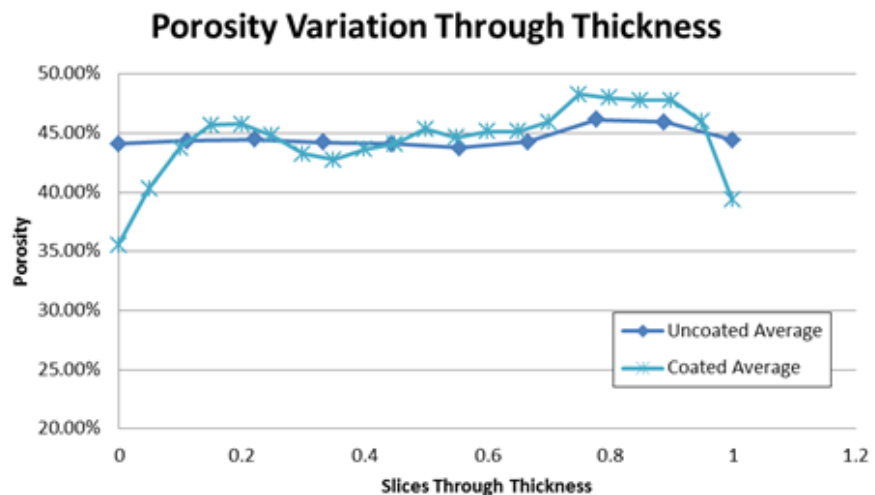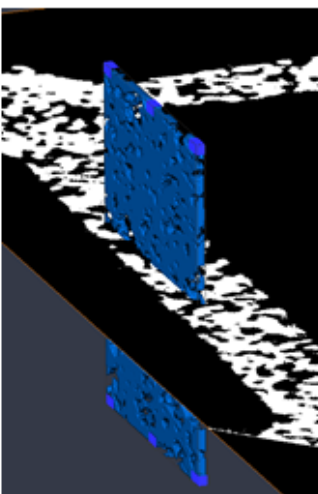
Figure 5.19: Porosity Variation Through Wall Thickness for Coated (Case 3) and Uncoated Filter (Case 2) Samples

The porosity variation through the thickness is calculated by taking small volume porosity slices through the thickness of the filter. The data shown is an average of four samples of each of the uncoated and coated filter walls. The greater variability of the coated porosity through the center portion of the wall thickness is due to the higher pore size distribution. A large pore size distribution can create local areas of either high or low porosity as a result of proximity to very large or very small pores. The existence of the washcoat resulted in up to an 8% decrease in filter porosity at either edge of the wall compared to the uncoated filter samples. The washcoat appears to penetrate about 15% of the way through the filter thickness. This is important because the ash particles only penetrate into the first ~10% of the filter so the effective porosity that the ash sees is the decreased porosity as a result of the washcoat. This is different from the nominal porosity specified for by the manufacturer that includes the porosity through the entire thickness. The ash interacting with the lower porosity surface region could have a large impact on deep bed filtration pressure drop.

5.2.4. Permeability Analysis

As mentioned previously, one of the goals for the advanced diagnostic analysis is to develop methods to scan ash and filter samples at a high enough resolution that the microstructure can be accurately reconstructed. This model could then be used in conjunction with flow simulation tools to calculate permeability on a variety of samples to directly quantify a range of effects on flow restriction. While the development of flow simulation tools and a comprehensive permeability analysis were outside the scope of this work, a number of test cases were run in a partnership with a pore flow simulation software to gauge the accuracy of the scanning methods and viability of these tools for further analysis. This pore flow simulation software utilizes the 3D segmented models as the input for simulation. These models can also be used on most commercial software as well as any tools developed later.

The initial test case consisted of a scan of the clean, uncoated cordierite filter material (Case 1) used in the ash cake layer experiments in section 4.1.1. The permeability of the sample value provided from the flow simulation software was 10.43×10^{-13} m^2 compared to an experimental clean permeability of 8.13×10^{-13} m^2 from the previous experiment. This agreement within 20%

is a significant improvement over initial, lower resolution estimates greater than an order of magnitude in difference. In addition, the current flow simulation software has limits on the volume of the sample to simulated. The volume is limited to a 250 x 250 x 250 voxel cube. At resolutions available from the reflection source, that is roughly a 300 μm cube or the size of the wall thickness. At the highest transmission source resolutions, that is only half of the thickness of the wall. As a result, local pore variation and selection of the simulation region can have a large effect on calculated permeability. Future studies will utilize improved software capabilities to incorporate larger regions for simulation and take a number of sections across the filter for a more accurate averaged permeability to compare with the much larger scale permeability measured experimentally. The accuracy with the test sample, however, does demonstrate the viability of the method for simulating sample permeability.

A number of other ash loaded samples were also simulated to compare with permeability estimations in [19]. While the scanned sample data includes ash both in the cake layer and deposited within the surface pores of the filter, the current flow simulation software is not capable of solving permeability for the high porosity regions of the ash cake layer. The segmented data is available for future simulation with updated software. As a result, the simulated permeability values are from samples of the filter wall with ash penetrating into the pores. This will be compared with the "wall permeability" in [19] which represents the calculated permeability from the initial pressure drop slope. Due to the low resolution nature of the pressure drop data with respect to ash loading, the slope of those pressure drop curves are calculated from two points. This makes the calculated permeability sensitive to the ash loading points at which the pressure drop was measured. Taking all of this into consideration, the comparison of the permeability values estimated from the pressure drop curves as described in [19] with the permeability values from this flow simulation over a number of samples is shown below in Table 5.2. Due to the extremely small volume of filter able to fit within the voxel restrictions, it is difficult to draw conclusions without first trying to understand the variation due to local porosity and the potential error from a lack of pressure drop resolution. The difference between the two permeability values vary from about 30% to over 300%.

Table 5.2: Comparison of Simulated Permeability from 3D Image Data with Previous Wall Permeability Calculations

Sample Type	Image Analysis Permeability (m^2)	Pressure Drop Calculated Permeability (m^2)
Field CJ-4	43.12×10^{-14}	n/a
Lab CJ-4	17.96×10^{-14}	4.98×10^{-14}
Lab Ca	12.73×10^{-14}	4.56×10^{-14}
Lab Mg	4.24×10^{-14}	5.82×10^{-14}

Significant additional study will be required to utilize this method for making concrete conclusions about the effects of lubricant additive chemistry and other ash properties on wall and cake layer permeability. Greater test sizes, thoughtful location selection, and averaging over a number of filter sections should all improve the reliability and accuracy of the permeability simulation results. These initial test cases have demonstrated the viability of this methodology for using high resolution 3D image data for the simulation of ash and filter permeability.

(Page intentionally left blank)

6. CONCLUSIONS AND FUTURE WORK

6.1. Compressed Ash Cake Layer Permeability

The ash cake layer regime in a DPF accounts for about 50% of the total ash related pressure drop over the life of the filter. The primary ash property that determines this flow restriction is the ash cake layer permeability. For typical CJ-4 derived ash, the packing density has a significant impact on the ash permeability. Over a wide packing density range seen in a filter of $0.15 - 0.75$ g/cm^3, the permeability varies over two orders of magnitude from 2.63 x 10^{-12} to 4.44 x 10^{-14} m^2. At a typical packing density of 0.3 g/L, a 50% decrease in packing density results in a factor of 10 increase in permeability and pressure drop. This represents a huge opportunity in improving permeability by even very small reductions in the ash packing density.

In addition, the lubricant additive chemistry also determines the permeability of the ash cake layer through the size, shape, and structure of the ash particles. At any given packing density point, the maximum difference in permeability due to ash chemistry was about an order of magnitude. The two types of ash with this large difference in permeability were the magnesium and calcium. The zinc and CJ-4 derived ash types fell in the middle of the spectrum. However, the spread between ash types or relative difference between permeability at a given packing density was not changed significantly by packing density. This means that the two effects are fairly independent which follows previous understandings that the ash structure primarily shifts the curve up or down while the shape of the curve is primarily driven by porosity/packing density. There is likely some small overlapping between the two effects as ash structure can affect packing density based on the operating conditions. Again, this provides an opportunity to reduce permeability through the formulation of lubricant additives to generate particles with ideal shapes.

6.2. Initial Pore Buildup Pressure Drop and Post Mortem Analysis

High resolution early ash loading in the deep bed filtration regime results in a linear increase in DPF pressure drop. Up to 3 g/L ash loading, there is no clear transition point in either the high magnesium or calcium ash loaded filters. The high magnesium loaded filters showed an average

increase in pressure drop of 0.35 kPa over that range from a baseline of 0.6 kPa. In comparison, the high calcium ash loaded filters only had an average increase in pressure drop of 0.30 kPa which demonstrates a much smaller difference in pressure drop as a result of ash chemistry compared to previous experiments. Over the runs for each ash type, the method demonstrated high repeatability.

In the post mortem analysis, the high magnesium ash loaded filter contained large spherical particles dispersed across the surface of the channel wall. The majority of the ash particles was deposited loosely within the surface pores and filled them near the point of the transition regime. The calcium ash particles clustered around the edges of the pores and contained dendritic structures that began to reach out over the pore opening, possibly as the beginning of pore bridging structures. The relatively smaller amount of ash particles within the pores signifies that the calcium ash loaded filters were still well within the deep bed filtration regime. The largely different deposition mechanisms still resulted in a similar pressure drop value.

6.3.   High Resolution X-Ray CT Imaging Method Development

A new method of mounting and scanning filter samples was developed in order to create extremely high resolution X-Ray CT images. Using single channel samples, a newly designed channel holder, and X-Y slider table to reduce wobble, resolutions from $0.62 - 1.25$ μm were achieved. This allowed for accurate reconstruction of the filter pore network and most of the deposited ash particles.

Using this high resolution data, accurate porosity values are able to be measured within the filter sample. There is a decrease in wall porosity of about 8% due to the presence of the washcoat compared to uncoated filters. This washcoat penetrates about 15% into the filter wall from either side. The high resolution data was segmented and reconstructed for input into a flow simulation module to test the capabilities of this resolution for permeability calculation. An uncoated test filter was calculated to have a permeability of 10.43×10^{-13} m^2 compared to an experimentally measured permeability of 8.13×10^{-13} m^2. This value within 20% came from a small sample of the same filter. Larger or more samples will provide a more representative value for the filter.

In addition, ash loaded sample data sets obtained using the higher resolution transmission source were also simulated and compared with previous low fidelity permeability estimations from full DPF pressure drop trends. The permeability values obtained from the flow simulation of these wall/ash samples varied from 4.24 x 10^{-14} to 43.12 x 10^{-14} m^2. These values were up to 3x higher than the estimations from the pressure drop curves. This is primarily due to the volume limitations from the current flow simulation software as well as the large error bars on ash loading level from the pressure drop curves.

6.4. Future Work and Recommendations

Using ash deposited onto wafer samples as a method of measuring permeability is very accurate and removes many of the variables associated with complex DPF geometry. While much information has been gained from measuring the permeability of previously generated ash, there are other operating variables that are not taken into consideration from this method. Ash generated and deposited onto a wafer sample in-situ will allow for the control of temperature, regeneration strategy, soot levels, and will prevent the ash layer from being disturbed through removal. In addition, permeability measurements can be taken at any point during the loading process. While the flow characteristics in this case differs slightly from that of the channel flow in the filter, it is a recommended next step to understand impacts from a number of other variables on ash cake layer permeability.

The high resolution loading of a filter within the deep bed filtration regime has presented important information on the high repeatability of the accelerated ash loading system. It has also provided important image analysis for the deposition differences between ash types. In order to better understand these differences and the location and impact of the transition point, it is recommended to load additional filters with the same ash types to increasing ash levels and section them for image analysis to understand the changes in ash deposition over time. Lower ash loading resolution can be used to decrease experimental time required while still capturing changes in pressure drop. In addition, the effect of soot loading level and regeneration strategy should be investigated on the different ash types.

In conjunction with the experimental setup used in the cake layer permeability testing, the new methods for generating high resolution X-Ray CT images will allow a new level of analysis for both lab and field samples. The image data, paired with simulation software will bridge the gap between microscale particle deposition analysis and quantifiable filter performance metrics. This can be used to better compare lab and field samples, understand the flow effects of local phenomena such as mid channel deposits and sintering, and continue to investigate lubricant additive formulations. Larger simulation volumes and more samples across the filter geometry will provide accurate information in order to support DPF performance improvements.

7. REFERENCES

[1] Heywood, J. B. (1988). *Internal Combustion Engine Fundamentals*. *McGrawHill series in mechanical engineering* (Vol. 21)

[2] DieselNet Technology Guide, "Diesel Engines", Revision 2013-12, DieselNet. <https://www.dieselnet.com/tech/diesel_engines.php>, 2013.

[3] DieselNet Technology Guide, "Emission Formation in Diesel Engines", Revision 2015, DieselNet. <https://www.dieselnet.com/tech/diesel_emiform.php>, 2015.

[4] American Lung Association of California, "Health Effects of Diesel Exhaust", <http://oehha.ca.gov/public_info/facts/pdf/diesel4-02.pdf>.

[5] Sappok, Alexander. "The Nature of Lubricant-derived Ash-related Emissions and their Impact on Diesel Aftertreatment System Performance." Massachusetts Institute of Technology, 16 Jun. 2009. Web. 20 Apr. 2015. .

[6] "Meeting EPA 2010." Facts About SCR. N.p., 2008. Web. 06 May 2016. <http://www.factsaboutscr.com/environment/epa2010.aspx>

[7] DieselNet Technology Guide, "What is Selective Catalytic Reduction", Revision 2005, DieselNet. <https://www.dieselnet.com/tech/cat_scr.php>, 2005.

[8] DieselNet Technology Guide, "Diesel Particulate Filters", Revision 2011, DieselNet. <https://www.dieselnet.com/tech/dpf.php>, 2011.

[9] Mogaka, Z.N., Wong, V.W., and Shahed, S.M., "Performance and Regeneration Characteristics of a Cellular Ceramic Diesel Particulate Trap," SAE 820272, 1982.

[10] Salvat 0., P. Marez and G. Belot, 2000. "Passanger Car Serial Application of a Particulate Filter System on a Common Rail Direct Injection Diesel Engine", SAE 2000-01-0473, 2000.

[11] Sappok, A., and Wong, V., "Detailed Chemical and Physical Characterization of Ash Species in Diesel Exhaust Entering Aftertreatment Systems", SAE 2007-01-0318, 2007.

[12] Konstandopoulos, A. G., Skaperdas, E., & Masoudi, M. (2002). Microstructural Properties of Soot Deposits in Diesel Particulate Traps. *SAE Technical Paper Series*, (724). http://doi.org/10.4271/2002-01-1015

[13] Sappok, A., & Wong, V. (2010). Ash Effects on Diesel Particulate Filter Pressure Drop Sensitivity to Soot and Implications for Regeneration Frequency and DPF Control. *SAE International 2010-01-0811*, *3*(1), 380–396. http://doi.org/10.4271/2010-01-0811

[14] Boschert, T., 2002. "The Lubricant Contribution to Future Low Emission Engine Design", Diesel Particulate and NOx Emissions Course (University of Leeds), Ann Arbor, MI,

October 2002.

[15] Rizvi, Syed Q.A., Lubricant Additives Chemistry and Aplications: Chapter 4. Detergents, CRC Press, 2003.

[16] McDonald, Randolph A., Lubricant Additives Chemistry and Applications: Chapter 2. Zinc Dithiophosphates, CRC Press, 2003.

[17] Dimou, I., Sappok, A., Wong, V., & Vogt, C. D. (2012). Influence of Material Properties and Pore Design Parameters on Non-Catalyzed Diesel Particulate Filter Performance with Ash Accumulation Hirofumi Sakamoto and Kazuya Yuuki. http://doi.org/10.4271/2012-01-1728

[18] Kosar, T. Fettah. X-ray MicroCT - Training Presentation. Cambridge, MA: Center for Nanoscale Systems - Harvard University, 19 Mar. 2013. PPT File.

[19] Wang, Y., Wong, V., Sappok, A., & Munnis, S. (2013). The Sensitivity of DPF Performance to the Spatial Distribution of Ash Inside DPF Inlet Channels. *Training*, *2014*, 4–10. http://doi.org/10.4271/2013-01-1584